A MODEL FOR FLOWS IN CHANNELS, PIPES, AND DUCTS AT MICRO AND NANO SCALES

Ali Beskok

Department of Mechanical Engineering, Texas A & M University, College Station, Texas, USA

George Em Karniadakis

Center for Fluid Mechanics, Brown University, Providence, Rhode Island, USA

Rarefied gas flows in channels, pipes, and ducts with smooth surfaces are studied in a wide range of Knudsen number (Kn) at low Mach number (M) with the objective of developing simple, physics-based models. Such flows are encountered in microelectromechanical systems (MEMS), in nanotechnology applications, and in low-pressure environments. A new general boundary condition that accounts for the reduced momentum and heat exchange with wall surfaces is proposed and its validity is investigated. It is shown that it is applicable in the entire Knudsen range and is second-order accurate in Kn in the slip flow regime. Based on this boundary condition, a universal scaling for the velocity profile is obtained, which is used to develop a unified model predicting mass flow rate and pressure distribution with reasonable accuracy for channel, pipe, and duct flows in the regime ($0 \leq Kn < \infty$). A rarefaction coefficient is introduced into this two-parameter model to account for the increasingly reduced intermolecular collisions in the transition and free-molecular regimes. The new model is validated with comparisons against direct-simulation Monte Carlo results, linearized Boltzmann solutions, and experimental data.

Rarefied internal gas flows are encountered in both low-pressure or vacuum environments as well as in micrometer or submicrometer size geometries at standard atmospheric conditions. Applications in the first category include devices used in hypersonic flight [1], and several types of vacuum instruments, e.g., ionization gauges, partial pressure and residual gas analyzers, etc. [2]. Applications in the second category are encountered in microelectromechanical systems (MEMS)

and include instrumentation, microelectronics, bioengineering, and advanced energy systems, where complex networks of microchannels may be used [3]. Similar applications can be found in the nanoscale design of computer components such as the modern Winchester-type hard disk drive mechanism, where the read/write head floats 50 nm above the surface of the spinning platter [4]. The head and platter together with the air layer in between form a slider bearing; both Reynolds and Mach number are very low (less than 0.6 and 0.3, respectively).

In these examples, the gas flow cannot be modeled based on the continuum hypothesis. The mean free path, which at standard atmospheric conditions is about 65 nm, is comparable to the characteristic geometric scale, and therefore microscopic effects are important. For example, in the case of the hard-drive mechanism which is modeled as a slider bearing, the load capacity predicted by the continuum Reynolds equations without slip is in error by more than 30% [5, 6]. The deviation of the state of the gas from continuum is measured by the Knudsen number (Kn), which is defined as $Kn = \lambda/L$, where λ is the mean free path of the molecules and L is a characteristic length scale. For the slider bearing the Knudsen number is $Kn = 1.3$; in ultralow clearances corresponding to increased recording capacity, the Knudsen number is well above 1. Similarly, ducts of width of 100 nm or less, which are common these days in nanotechnology applications, correspond to Knudsen number above 1. In other capillary flows, such as in helium leak detection devices and mass spectrometers, the Knudsen number may achieve values up to 200 [7]. Finally, material processing applications such as chemical vapor deposition (CVD) and molecular beam epitaxy applications also involve high Knudsen number flow regimes [8].

As the value of Knudsen number increases, rarefaction effects become more important and thus pressure drop, shear stress, heat flux, and corresponding mass flow rate cannot be predicted from standard flow and heat transfer models based on the continuum hypothesis. On the other hand, simple models based on kinetic gas theory concepts are not appropriate either, except in the very high Knudsen number regime corresponding to near-vacuum conditions [9]. The appropriate flow and heat transfer models depend on the range of the Knudsen number. A classification of the different flow regimes is given by [10]: for $Kn \leqslant 10^{-3}$ the fluid can be considered as a continuum, while for $Kn \geqslant 10$ it is considered a free molecular flow. A rarefied gas can neither be considered an absolutely continuous medium nor a free molecular flow in the Knudsen number range between 10^{-3} and 10. In that region, a further classification is needed, i.e., slip flow ($10^{-3} < Kn < 0.1$) and transition flow ($0.1 < Kn < 10$). This classification is based on empirical information and thus the limits between the different flow regimes may depend on the problem geometry. A verification of this taxonomy based on experimental data has been documented in [11]. In a long micropipe with a large pressure ratio from inlet to outlet, all three flow regimes may coexist as rarefaction is increased along the flow direction. This means that a very large variation of scales may be present from the continuum at the inlet of the micropipe to free molecular flow at the outlet. Such cases are achieved in vacuum experiments, where very large pressure gradients are imposed on capillaries exhausting to high-vacuum conditions (see Figure 5 in [7]).

Experimental data as well as theoretical work have demonstrated a nonlinear dependence of mass flow rate on the pressure drop for the slip flow regime [12]. The mass flow rate scales more closely with the difference of inlet and exit pressures squared, which is characteristic of *compressible* flows in long channels. This was also verified in the slip flow experiments of [13] in short pipes with a diameter of 2 in. (5 cm) at low pressures. Similarly, for flows in microchannels in recent experiments by Liu et al. [14] and Pong et al. [15], the pressure distribution along the microchannel was measured by using a surface micromachined system with a number of sensors as part of the surface; a nonlinear pressure distribution was clearly demonstrated in these experiments.

The flow rate in isothermal rarefied flows is increased compared to the continuum-based estimates. This has also been documented in a number of experimental studies for flows in microscales. The first known experiment of flow in microchannels was performed by Gaede [16], who placed two parallel plates 4 μm apart. Gaede found that the flow rate of hydrogen decreases about 60% from the free molecular value while passing through a minimum and then rising with increasing pressure levels. In long capillaries, the difference between the minimum and the free molecular value is only 5–8%. Therefore, rarefied flows behave differently in pipes and channels.

Driven by MEMS applications, a number of experimental studies with microchannels have been conducted. The first recent experimental study of a slip flow using micromachined channels was conducted for both gases and liquids by Pfahler et al. [17] and Harley et al. [18] in a Reynolds number range $0.50 \leqslant Re \leqslant 20$ and Knudsen number range $0.001 \leqslant Kn \leqslant 0.363$. The reported skin friction reduction due to apparent slip of the flow has been confirmed in other similar experimental studies [14, 15, 19] using different microfabrication techniques to fabricate the microchannels.

1 OBJECTIVES

While significant progress has been made both experimentally and theoretically for the slip and the free-molecular flow regimes, there is lack of theoretical understanding and therefore of reliable models, especially in the *transition* regime. The classical Knudsen's model, which has been used extensively in vacuum science, is valid for transitional and free molecular flows in pipes but overpredicts mass flow rate in the slip flow regime. Knudsen's model is based on two free parameters, which are adjusted to fit measurements of flow rate. There is currently no model for predicting corresponding velocity profiles nor pressure distribution in the *entire* Knudsen number regime. Moreover, there is no such model that can be used in other geometries, e.g., two-dimensional channels and rectangular ducts with different aspect ratios. The objective of the current investigation is to develop a unified, physics-based model appropriate for all rarefaction regimes and for general internal geometries, i.e., pipes, two-dimensional channels, and ducts. We consider both microflows as well as nanoflows, excluding nonclassical effects and considering smooth surfaces only. To this end, we use a mix of results based on continuum-based

models, atomistic simulations, solutions of the Boltzmann equation, and experimental results to validate the proposed model.

The numerical investigation of rarefied flows necessitates either using atomistic (particle-based) simulations or adding approximate corrections to the macroscopic simulation methods. For example, in the slip flow regime it is reasonable to employ the Navier-Stokes equations modified at the surface with appropriate velocity-slip conditions [10]. In previous work, in a series of articles [11, 20, 21], we developed compressible and incompressible flow models with high-order velocity-slip boundary conditions for the slip flow regime. In the current work we examine the validity of a *general* slip boundary condition we propose for the entire Knudsen number regime by comparing the predictions of the new slip model with the direct-simulation Monte Carlo (DSMC) method of Bird [22] and solutions of linearized Boltzmann equations [23, 24]. Based on successful representation of the velocity distribution in the entire flow regime, we propose a *unified* model that is capable of predicting the volumetric and mass flow rate as well as the pressure distribution accurately. This model is based on a generalized rarefaction coefficient, which depends on two parameters, and can be obtained from either theory and simulations or from experimental data.

The article is organized as follows: In Section 2 we present the governing equations and slip models for slip and transitional flow regimes and summarize the computational methods employed in our investigation. In Section 3 we concentrate on channel flows in the slip and transition flow regimes and provide appropriate scaling laws for the velocity and mass flow rate. In Section 4 we use experimental and numerical data for pipe and rectangular cross-section duct flows in order to validate the proposed model. Special emphasis is placed in modeling the entire flow regime accurately. We conclude in Section 5 with a summary and a discussion of our results.

2 GOVERNING EQUATIONS AND SLIP MODELS

In the slip flow regime $(0.001 < \text{Kn} < 0.1)$, deviations from the state of continuum are relatively small and the flow is still governed by the Navier-Stokes equations [10]. The rarefaction effect is modeled through the partial slip at the wall using slip boundary conditions [25]. Although internal rarefied gas flows can be modeled as *isothermal*, the *compressible* Navier-Stokes equations are more appropriate since large pressure variations are experienced in these flows [11, 13, 14, 15]. In this section we will develop a general boundary condition for velocity slip, which in the case of $\text{Kn} < 1$ corresponds to a second-order correction in Knudsen number, improving Maxwell's original first-order formula.

The Navier-Stokes equations break down in the transition regime $(\text{Kn} > 0.1)$ and have to be substituted either by the Boltzmann equation, which is valid at the microscopic level or by continuum approximations (e.g., the Burnett or Woods equations) that include high-order modifications of the stress tensor and heat flux terms [26, 27]. In particular, a number of investigators have considered semianalytical and numerical solutions of the linearized Boltzmann equations for rarefied flow between two parallel plates and a pipe. Starting with the pioneering work of Cercignani and his associates, the Knudsen's minimum was rigorously investigated

for the first time [28]. Simplifications for the collision integral based on the Bhatnagar-Gross-Krook model [29] were used extensively in such studies. Other investigators have derived solutions based on the hard sphere and Maxwellian models for the collision integral [23, 30], and have also obtained solutions in cylindrical geometry [24], and on ducts with various cross sections [23, 31]. Similar approaches have been used successfully in modeling gas film lubrication in the transition regime [5].

Numerically, for gas flows it is more efficient to use the DSMC method of [22] to obtain solutions in the transition regime. DSMC is a particle-based method, and uses a stochastic algorithm to evaluate collision probabilities and scattering distributions, avoiding expensive molecular dynamics-type simulations where the exact trajectories of all particles are computed. In recent work by Wagner [32], it has been rigorously proved that DSMC is equivalent to a Monte Carlo solution of an equation "close" to the Boltzmann equation; statistical error analysis for DSMC has been investigated by Chen and Boyd [33]. A modified Boltzmann algorithm has been used recently in successfully modeling rarefaction in the gas film lubrication problem [34]. Oh, Oran, and Cybyk [35] have used the DSMC method to investigate subsonic and transonic flows in microchannels. More recently, hybrid schemes combining DSMC and Navier-Stokes representations have been developed [36]. In the current work, we will use Bird's version of DSMC to simulate rarefied flows in channels.

2.1 First-Order Models

By first-order models we refer to the approximation of Boltzmann equation up to $\mathcal{O}(\mathrm{Kn})$, i.e., the compressible Navier-Stokes equations. The conservation equations for mass, momentum, and energy are

$$\frac{\partial}{\partial t}\begin{bmatrix} \rho \\ \rho u_i \\ e \end{bmatrix} + \frac{\partial}{\partial x_j}\begin{bmatrix} \rho u_j \\ \rho u_i u_j + p\delta_{ji} - \sigma_{ji} \\ e u_j + (p\delta_{ij} - \sigma_{ji})u_i + q_j \end{bmatrix} = 0 \tag{1}$$

where ρ and p are the gas density and pressure, respectively. The velocity components in two dimensions are denoted by $(u_1, u_2) \equiv (u, v)$ in the Cartesian coordinate system $(x_1, x_2) \equiv (x, y)$. The ideal gas assumption is used to determine pressure in terms of local density and temperature, i.e., $p = \rho RT$, where R is the specific gas constant, and the temperature is determined from $e = \rho(C_v T + (u_i u_i)/2)$, where C_v is the specific heat at constant volume.

The conservation equations (1) are valid for continuum as well as for rarefied flows. However, the viscous stresses (σ_{ij}) and the heat flux (q_i) have to be determined differently for different flow regimes. For the first-order model they have the familiar forms used in the Navier-Stokes equations,

$$\sigma_{ij}^{N-S} = \mu\left(\frac{\partial u_j}{\partial x_i} + \frac{\partial u_i}{\partial x_j}\right) - \frac{2}{3}\mu\frac{\partial u_m}{\partial x_m}\delta_{ij} \tag{2}$$

where μ is the dynamic viscosity and δ_{ij} is the Kronecker delta. The heat flux is determined from the Fourier law $q_i = -\kappa(\partial T/\partial x_i)$, where κ is the thermal conductivity.

In the *slip flow* regime, the Navier Stokes equations (1), (2) are solved subject to the velocity slip and temperature jump boundary conditions given by

$$u_s - u_w = \frac{2-\sigma_v}{\delta_v}\frac{1}{\rho(2RT_w/\pi)^{1/2}}\tau_s + \frac{3}{4}\frac{\Pr(\gamma-1)}{\gamma\rho RT_w}(-q_s) \tag{3}$$

$$T_s - T_w = \frac{2-\sigma T}{\sigma_T}\left[\frac{2(\gamma-1)}{\gamma+1}\right]\frac{1}{R\rho(2RT_w/\pi)^{1/2}}(-q_n) \tag{4}$$

where q_n, q_s are the normal and tangential heat flux components at the walls. Also, τ_s is the viscous stress component corresponding to the skin friction, γ is the ratio of specific heats, u_w and T_w are the reference wall velocity and temperature, respectively. Pr is the Prandtl number. [Equation (3) was proposed by Maxwell in 1879.] The second term in Eq. (3) represents the thermal-creep contribution to slip velocity, which describes flow from the cold toward the hot direction along nonisothermal surfaces. This phenomenon has been studied in some detail in [12, 21]. Since we consider here only isothermal surfaces, the second term in Eq. (3) is zero. Equation (4) is due to von Smoluchowski [25] and models temperature jump effects. Here σ_v, σ_T are the tangential momentum and energy accommodation coefficients, respectively. The accommodation coefficients model the momentum and energy exchange of the gas molecules impinging on the walls. They are dependent on the specific gas and the surface quality and are tabulated (see, for example, [37]); under laboratory conditions, values as low as 0.2 have been observed [38]. Very low values of σ_v will increase the slip on the walls considerably even for small Knudsen number flows, due to the $(2-\sigma_v)/\sigma_v$ factor.

Our derivation of high-order slip boundary condition is based on tangential momentum flux analysis near an isothermal surface (for details, see [39]), which results in the following relation:

$$u_s = \frac{1}{2}[u_\lambda + (1-\sigma_v)u_\lambda + \sigma_v u_w] \tag{5}$$

where u_s is the slip velocity near the surface, u_λ is the tangential component of gas velocity one mean free path away from the surface, and u_w is the tangential velocity of the surface. Notice that instead of obtaining the slip information u_λ exactly λ away from the wall, a fraction of λ may be used [9]. Using a Taylor series expansion for u_λ about u_s, rearranging, and nondimensionalizing with a reference length and a velocity scale (such as free-stream velocity), we obtain

$$U_s - U_w = \frac{2-\sigma_v}{\sigma_v}\left[\mathrm{Kn}\left(\frac{\partial U}{\partial n}\right)_s + \frac{\mathrm{Kn}^2}{2}\left(\frac{\partial^2 U}{\partial n^2}\right)_s + \dots\right] \tag{6}$$

where the nondimensional quantities are denoted by capital letters. By neglecting the higher-order terms in the above equation we recover Maxwell's first-order slip boundary condition (3) in nondimensional form.

2.2 Second-Order Models

The conservation equations (1) are still valid for larger deviations from equilibrium conditions, but the stress tensor (and heat flux vector) have to be corrected for high-order effects. The general tensor expression of the Burnett level shear stress is

$$
\sigma_{ij}^B = -2\mu \overline{\frac{\partial u_i}{\partial x_j}} + \frac{\mu^2}{p}\left[\omega_1 \overline{\frac{\partial u_k}{\partial x_k} \frac{\partial u_i}{\partial x_j}} + \omega_2 \left(\overline{\frac{D}{Dt} \frac{\partial u_i}{\partial x_j}} - 2 \overline{\frac{\partial u_i}{\partial x_k} \frac{\partial u_k}{\partial x_j}} \right) \right.
$$

$$
\left. + \omega_3 R \overline{\frac{\partial^2 T}{\partial x_i \partial x_j}} + \omega_4 \frac{1}{\rho T} \overline{\frac{\partial p}{\partial x_i} \frac{\partial T}{\partial x_j}} + \omega_5 \frac{R}{T} \overline{\frac{\partial T}{\partial x_i} \frac{\partial T}{\partial x_j}} + \omega_6 \overline{\frac{\partial u_i}{\partial x_k} \frac{\partial u_k}{\partial x_j}} \right] \quad (7)
$$

where a bar over a tensor designates a nondivergent symmetric tensor, i.e., $\overline{f_{ij}} = (f_{ij} + f_{ji})/2 - \delta_{ij}/3 f_{mm}$. Similar expressions are valid for the heat flux q_i^B [40]. The difference here is that we use the exact definition of the *total derivative* instead of the Euler approximation most commonly used in hypersonic rarefied flows. The coefficients ω_i depend on the gas model and have been tabulated for hard spheres and Maxwellian gas models [40, 41].

To simplify the stress tensor we consider a very long channel of length L and height h so that $\varepsilon \equiv h/L \ll 1$. We also neglect any temperature gradients in the gas (isothermal wall conditions and low subsonic flow are assumed). Under such conditions the Burnett equations can be simplified considerably, resulting in terms including $\mathcal{O}(1)$ up to $\mathcal{O}(\varepsilon^5)$. For convenience, results of this expansion including $\mathcal{O}(\varepsilon)$ terms are given in the Appendix. In that limit, the x-momentum equation is reduced to

$$
\frac{\partial p}{\partial x}\left[1 - \left(\frac{\omega_2}{3} + \frac{\omega_6}{12} \right) \frac{\mu^2}{p^2} \left(\frac{\partial u}{\partial y} \right)^2 \right] = \mu \frac{\partial^2 u}{\partial y^2} + \mathcal{O}(\varepsilon) \quad (8)
$$

Furthermore, assuming a Maxwellian gas model for which $(\omega_1, \omega_2, \omega_6) = (10/3, 2, 8)$ and nondimensionalizing with reference exit conditions (p_0, u_0) we obtain in nondimensional form

$$
P_x\left[1 - \frac{2\gamma\pi}{3} \text{Kn}_0^2 M_0^2 \left(\frac{p_0^2}{p} \right)(U_y)^2 \right] = U_{yy} + \mathcal{O}(\varepsilon) \quad (9)
$$

Similarly, for the y-momentum equation we obtain

$$P_y \left[1 + \frac{\gamma \pi}{3} \mathrm{Kn}_0^2 \, M_0^2 \left(\frac{p_0}{p} \right)^2 (U_y)^2 \right] = \frac{4}{3} \sqrt{\frac{\gamma \pi}{2}} \, M_0 \, \mathrm{Kn}_0 \left(\frac{p_0}{p} \right) U_y U_{yy} + \mathcal{O}(\varepsilon) \quad (10)$$

It is clear that the $M_0^2 \mathrm{Kn}_0^2 (p_0/p)^2$ terms are relatively small for small Mach number flows in the early transition regime (i.e., $\mathrm{Kn} \simeq 1$). In this case, for flow in a very long channel the Burnett equations reduce to

$$P_x = U_{yy}$$

$$P_y = \frac{4}{3} \sqrt{\frac{\gamma \pi}{2}} \, \mathrm{Kn}_0 \, M_0 \left(\frac{p_0}{p} \right) U_y U_{yy}$$

Therefore, the streamwise momentum Burnett equation is reduced to the form obtained by the Navier-Stokes equations in that limit. The crossflow momentum equation shows that the pressure gradient in that direction is balanced by the Burnett normal stresses, which in the case of continuum are identically zero for a flat surface. The above equations agree with the simplified set of equations for Couette flow in the transition regime obtained by Schamberg [41].

Since the Burnett equations are obtained by a second-order Chapman-Enskog expansion in Kn, they require second-order slip boundary conditions. Such boundary conditions were derived by Schamberg in [41]; however, numerical experiments with aerodynamic rarefied flows [40] showed that Schamberg's boundary conditions are inaccurate for $\mathrm{Kn} > 0.2$. Based on our analysis in Section 2.1, we propose the following second-order slip boundary condition:

$$U_s - U_w = \frac{2 - \sigma_v}{\sigma_v} \left[\mathrm{Kn} \left(\frac{\partial U}{\partial n} \right)_s + \frac{\mathrm{Kn}^2}{2} \left(\frac{\partial^2 U}{\partial n^2} \right)_s \right] \quad (11)$$

Similar second-order slip boundary conditions have also been proposed by Deissler [42] and Cercignani and used in [13] for a pipe or a channel flow in the following form:

$$U_s - U_w = C_1 \, \mathrm{Kn} \left(\frac{\partial U}{\partial n} \right)_s - C_2 \, \mathrm{Kn}^2 \left(\frac{\partial^2 U}{\partial n^2} \right)_s$$

where $(\partial/\partial n)$ shows gradients normal to the wall surface. The slip coefficients are $C_1 = 1.0$, $C_2 = 1.6875$ according to [42], and $C_1 = 1.1466$, $C_2 = 0.9756$ according to Cercignani [13]. In experimental work by measuring the mass flow rate, Sreekanth [13] reports good agreement of second-order slip boundary conditions with his results for Kn as high as $\mathrm{Kn} = 1.5$. However, Sreekanth used a different second-order slip coefficient ($C_2 = 0.14$) than the ones proposed by Deissler (1.6875) and Cercignani (0.9756). He also reports a change of the first slip coefficient (C_1) from 1.00 to 1.1466 as the Knudsen number is increased. First-order boundary conditions cease to be accurate, according to Sreekanth's study, above $\mathrm{Kn} > 0.13$. More

recent studies by [43] also show that Maxwell's slip boundary condition breaks down around $Kn = 0.15$.

Implementation of second-order slip boundary condition using Eq. (11) requires obtaining the second derivative of the tangential velocity in the normal direction to the surface ($\partial^2 U / \partial n^2$), which may lead to computational difficulties, especially in complex geometry configurations. To circumvent this difficulty we propose the following general velocity slip boundary condition:

$$U_s - U_w = \frac{2 - \sigma_v}{\sigma_v} \left[\frac{Kn}{1 - b\,Kn} \left(\frac{\partial U}{\partial n} \right)_s \right] \tag{12}$$

where b is the slip coefficient, which is an empirical parameter to be determined either experimentally or from linearized Boltzmann or DSMC data. For a slightly rarefied flow corresponding to small Kn, using asymptotic expansions of the velocity field, the following expression for b is obtained to ensure second-order accuracy [44]:

$$b = \left(\frac{1}{2} \frac{U_0''}{U_0'} \right)_s = \frac{1}{2} \left[\frac{(\partial \omega / \partial n)_0}{\omega_0} \right]_s$$

where the subscript 0 refers to the corresponding continuum field (zeroth-order of the expansion). Note that the second-order derivative of the (continuous) velocity field as shown in Eq. (12) is absorbed in the parameter b. Moreover, parameter b has a physical meaning: it is the vorticity flux into the surface divided by the vorticity of flow field on the surface, obtained by the no-slip approximation. For fully developed flows in channels, $b = -1$.

We should also note here that Eq. (12) predicts finite slip contributions as $Kn \to \infty$. Therefore, this boundary condition may be valid (with consistent values of b) for the entire Knudsen flow regime, while the other slip models diverge with increasing Kn.

2.3 Summary of Computational Models

We have developed a spectral element algorithm μ**Flow** [39] for solution of compressible, subsonic Navier-Stokes equations. This algorithm is based on time splitting of advection and diffusion operators, which are treated with a collocation formulation and Galerkin projection, respectively. The element-interface connectivity conditions are handled by a characteristic decomposition for the advection substep, and a direct stiffness summation is employed at the diffusion substep. The computational domain is broken up into K macroelements, and the dependent and the independent variables are approximated by Nth-order tensor-product polynomial expansions. Convergence to the exact solution is achieved by varying either the number of macroelements K or the polynomial order N. It is the latter approach that results in exponentially fast convergence (spectral accuracy), while the former approach corresponds to fixed, finite-element-like accuracy. The slip

flow regime is investigated by implementing the slip boundary condition (5) and a corresponding temperature-jump boundary condition. The spectral element code is restricted to shock-free flows, therefore it is used for subsonic and shock-free transonic flows. Resolution tests and grid-independent solutions have been verified for all simulations and details will be presented in Section 3 for representative cases.

In addition, we use the DSMC code of Bird [22] with certain modifications for our geometries. The DSMC code requires the accommodation coefficients (σ_v, σ_T) to model the interaction of the molecules with the surfaces. This algorithm simulates the slip effects without defining a set of continuum-based slip conditions. Although the DSMC methods are appropriate for simulating rarefied flows, they have some disadvantages. One main disadvantage is that the error of the method is inversely proportional to the square root of the number of simulated molecules. In addition, low-Mach-number flow simulations require a large number of time averagings / samplings, making the DSMC method very expensive. The reason for this is the smallness of mean flow properties (such as average flow speed) for low subsonic flows compared to the molecular magnitudes, which are of the order of speed of sound. In these cases, our results are sampled for a long time.

The DSMC simulations are performed for channels with length-to-height ratio $L/h = 20$. The domain is discretized with 6,000 cells, 200 in the streamwise and 30 in the cross-flow direction. With this discretization we used 80,000 molecules and sampled our results for 2.0×10^6 time steps. We have performed resolution studies by first increasing the number of simulated molecules to 240,000 and sampling the results for 2.5×10^5 time steps. We also simulated cases with 24,000 cells by employing 400 cells in the streamwise direction and 60 cells across the channel. A total of 480,000 molecules were simulated, and the results were sampled for 1.0×10^5 time steps. For the previous simulations we have used the variable hard sphere (VHS) model. We repeated some of our simulations (24,000 cells and 480,000 simulated molecules cases) with the variable soft sphere (VSS) model. These cases were also sampled for 1.0×10^5 time steps. Both the VSS and the VHS simulations resulted in identical solutions, as expected since we considered isothermal flows.

## 3 CHANNEL FLOWS

3.1 Slip Flow Regime

The slip flow regime $(0.001 < \text{Kn} < 0.1)$ has been studied systematically by Beskok et al. [11, 21]. Here we present some μ**Flow** simulations and a comparison with DSMC results for a microchannel with length-to-height ratio ($L/h = 20$) and inlet-to-exit pressure ratio $\Pi = 2.28$. The Knudsen number at the channel outlet is 0.20. The discretization corresponds to 10 elements in the flow direction and 2 elements in the crossflow direction, employing 6th-order polynomial expansions per direction in each element. Convergence is verified by increasing the order of the polynomial expansions while keeping the number of spectral elements fixed (p-refinement). In addition, we monitor the residuals of the global conservation of mass and momentum. The results presented in these runs conserve mass and

momentum with 0.01% accuracy. The DSMC results correspond to $\Pi = 2.28$ with resolution parameters as discussed in Section 2.3. Convergence is also verified by monitoring mass balance; maximum errors are approximately 1%. Velocity profiles for $\Pi = 2.28$ at three different x/L locations (nondimensionalized with the reference inlet velocity), are plotted in Figure 1. Parabolic velocity distribution is obtained across the channels. Both the DSMC and μ**Flow** predict the same magnitude of velocity. Pressure and slip velocity distributions are also in good agreement.

Implementation of our second-order model in the slip flow regime was done by obtaining the necessary slip information at a distance λ away from the surface in Eq. (5). In this regime, the results are identical with those obtained using Eq. (12). However, for flows with higher Knudsen number in the transition regime, we switch our model to the general boundary condition of Eq. (12), the validity of which we investigate next in detail.

3.2 Transition and Free Molecular Flow Regimes

It is known from Knudsen's and Gaede's experiments in the transition flow regime that there is a minimum in the flow rate in pipe and channel flows at about $Kn \simeq 3$ and $Kn \simeq 1$, respectively. This behavior has been investigated by many
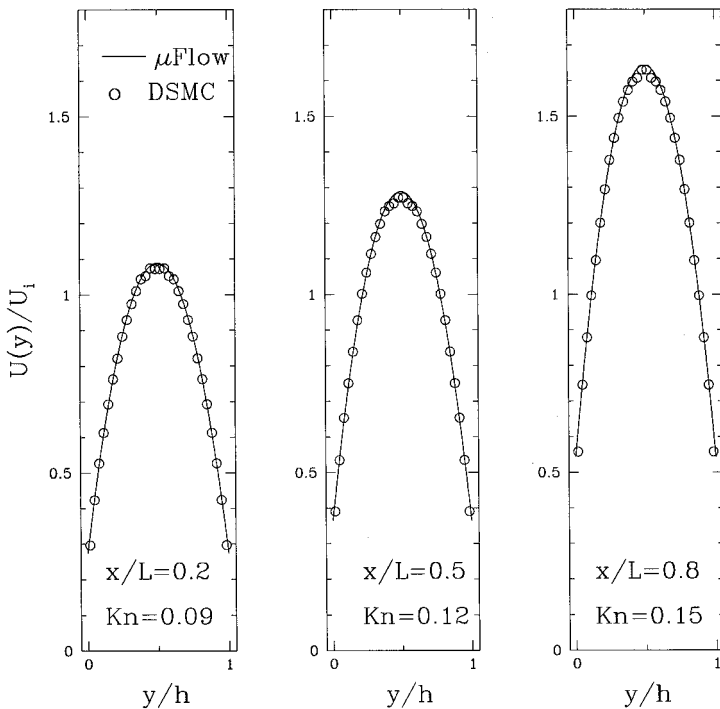
Figure 1. Velocity profiles predicted by the Navier-Stokes and DSMC simulations at various x/L locations. The inlet is located at $x/L = 0.0$.

researchers both theoretically [23, 24, 28, 45–47] and experimentally [7]. It was first shown by Knudsen that in the free molecular flow regime in pipes a diffusive transport process proportional to the pressure gradient but independent of density is observed. Accordingly, the free molecular mass flow rate in pipes is [25]

$$\dot{M}_{FM} = \frac{4}{3} a^3 \frac{\Delta P}{L} \left(\frac{2\pi}{RT} \right)^{1/2}$$

(13)

Deviation from this behavior is expected for finite-length pipes (i.e., $a \ll L \ll \lambda$) by a factor $(1 - ca/L)$ (up to first order in a/L) due to the end effects [46], where c is a constant. However, for free molecular flow in two-dimensional very long channels ($h \ll \lambda \ll L$), the flow rate asymptotes a value proportional to $(1/\pi)^{1/2}$ $\log_e(Kn)$ as $Kn \to \infty$ [45, 48]. This logarithmic behavior is attributed to the degenerate geometry of the two-dimensional channel [47]. For two-dimensional channels of finite length, the flow rate tends toward a finite limit (see the discussion of D. R. Willis at the end of [45]). For ducts, the flow rate tends toward a finite limit, thus resembling pipe flow behavior. This has been documented in the experiments of Gaede and verified by the linearized Boltzmann solutions [49].

The variation of flow rate in a channel, obtained by DSMC simulations in the transition and early free molecular flow regimes, is shown in Figure 2. The volumetric flow rate data are presented at the average Knudsen number in the channel (corresponding to the mean pressure $\overline{P}$ between the inlet and outlet), and it is nondimensionalized in the following form:

$$\overline{Q} = \frac{\dot{Q}\overline{P}}{(-dP/dx)h^2(RT_0)^{1/2}}$$

where $\dot{Q}$ is the volumetric flow rate per unit width of the channel, h is the channel height, T_0 is reference temperature, and R is the specific gas constant. The DSMC data is incorporated into the figure by plotting the mass flow rate data as a function of average Kn in the channel, since $\dot{M} \approx \dot{Q}\overline{P}$. The error bars in the plot correspond to maximum fluctuations in the global mass balance and statistical scatter in pressure gradient (dP/dx), which is used here as an accuracy criterion. The Knudsen's minimum is clearly captured by the DSMC results at $Kn \simeq 1.0$. The DSMC solution is compared with the semianalytic solutions of Cercignani and Daneri [28], where the linearized Boltzmann equations are solved with the BGK model. Also, a comparison with numerical solutions of Huang et al. is shown [30]. These solutions were obtained from the linearized Boltzmann equations with the BGK model using the discrete ordinate method; the integrals involved were approximated by various orders of Gauss quadrature (n). It is seen that Cercignani and Daneri's results are recovered as the quadrature order (n) is increased. The current DSMC results match the Boltzmann solution quite well up to $Kn = 2$. Beyond this value, the DSMC results follow the $n = 7$ order quadrature solution in [30], and subsequently asymptote to a constant value in the free molecular flow regime, rather than increasing logarithmically. The reason for deviations of the
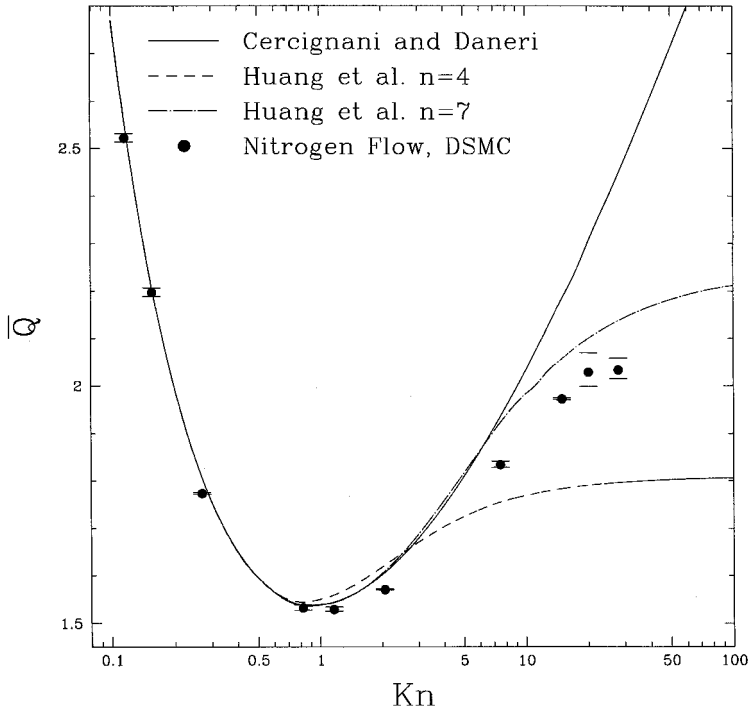
Figure 2. Variation of normalized flow rate in a channel as a function of Knudsen number. Comparisons are made between DSMC results and solutions of the linearized Boltzmann equation.

DSMC data from the theoretical solution for infinitely long channels is obviously the finite length of the channel ($L/h = 20$) used in these simulations.

3.2.1 Velocity scaling. From DSMC results and solutions of the linearized Boltzmann equation, it is evident that velocity profiles remain approximately parabolic for a large range of Knudsen number (see Figure 3). This is also consistent with the analysis of Navier-Stokes and Burnett equations in long channels as documented in Section 2.2. Based on this observation we can then start with a parabolic velocity profile and write the dimensional form for velocity distribution in a channel of thickness h:

$$U(x, y) = \mathscr{F}\left(\frac{dP}{dx}, \mu_0, h, \lambda\right)\left[-\left(\frac{y}{h}\right)^2 + \left(\frac{y}{h}\right) + \left(\frac{2 - \sigma_v}{\sigma_v}\right)\frac{\text{Kn}}{1 - b\,\text{Kn}}\right]$$

where $\mathscr{F}[(dP/dx), \mu_0, h, \lambda]$ shows functional dependence of velocity on the pressure gradient, viscosity, channel height, and local mean free path. The temperature is assumed to be constant and therefore the dynamic viscosity is also a constant. The last term represents the contribution of the slip velocity, and it is given by Eq. (12) with $U_w = 0$. Assuming this form of velocity distribution, the average velocity
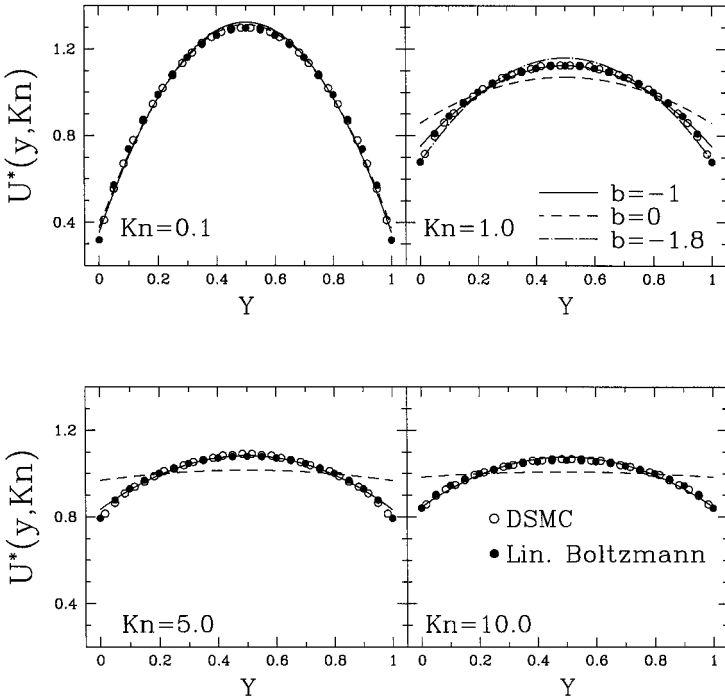
Figure 3. Velocity profile comparisons of the model [Eq. (14)] with DSMC and linearized Boltzmann solutions [23]. Maxwell's first-order boundary condition is shown with dashed lines ($b = 0$), and general slip boundary condition ($b = -1$) is shown with solid lines.

in the channel ($\overline{U} = \dot{Q}/h$) can be obtained as

$$\overline{U}(x) = \mathscr{F}\left(\frac{dP}{dx}, \mu_0, h, \lambda\right)\left[\frac{1}{6} + \left(\frac{2 - \sigma_v}{\sigma_v}\right)\frac{Kn}{1 - b\,Kn}\right]$$

By nondimensionalizing the velocity distribution with the local average velocity, the dependence on local flow conditions, $\mathscr{F}[(dP/dx), \mu_0, h, \lambda]$, is eliminated. Therefore, the resulting relation is a function of Kn and y only. Assuming $\sigma_v = 1$ (for simplicity), we obtain

$$U^*(y, Kn) \equiv U(x, y)/\overline{U}(x) = \left[\frac{-(y/h)^2 + (y/h) + Kn/(1 - b\,Kn)}{(1/6) + Kn/(1 - b\,Kn)}\right] \quad (14)$$

A similar analysis has been performed by Piekos and Breuer [43], who used the first-order slip boundary conditions and subsequently separated this equation into an x-dependent contribution and a y-dependent contribution to investigate the breakdown of slip flow theory. Here, however, we will keep the form of Eq. (14) in the following analysis. In Figure 3 we plot the nondimensional velocity variation

obtained in a series of DSMC simulations for Kn = 0.1, Kn = 1.0, Kn = 5.0, and Kn = 10.0. We have also included the corresponding linearized Boltzmann solutions in [23]. It is seen that the DSMC velocity distribution and the linearized Boltzmann solutions agree quite well. We can now use Eq. (14) and compare with the DSMC data, by varying the parameter b, which for $b = 0$ corresponds to Maxwell's first-order and for $b = -1$ to the second-order boundary condition in the *slip regime* only. Here we find that for $b = -1$, Eq. (14) results in an accurate model of the velocity distribution for a wide range of Knudsen number. It is clear that the slip velocity is slightly overestimated with our model for the Kn = 1.0 case. To obtain a better slip velocity, we varied the value of the parameter b by imposing, for example, $b = -1.8$ for the Kn = 1.0 case. Although a better agreement is achieved for the slip velocity, the accuracy of the model in the rest of the channel is destroyed.

In Figure 4 we show the nondimensionalized velocity distribution along the centerline and along the wall of the channels for the entire Knudsen number regime considered here, i.e., 0.01 ⩽ Kn ⩽ 30. We have included in the plot data for the slip velocity and centerline velocity from 20 different DSMC runs, of which 15 of them were for nitrogen (diatomic molecules), and 5 of them were for helium
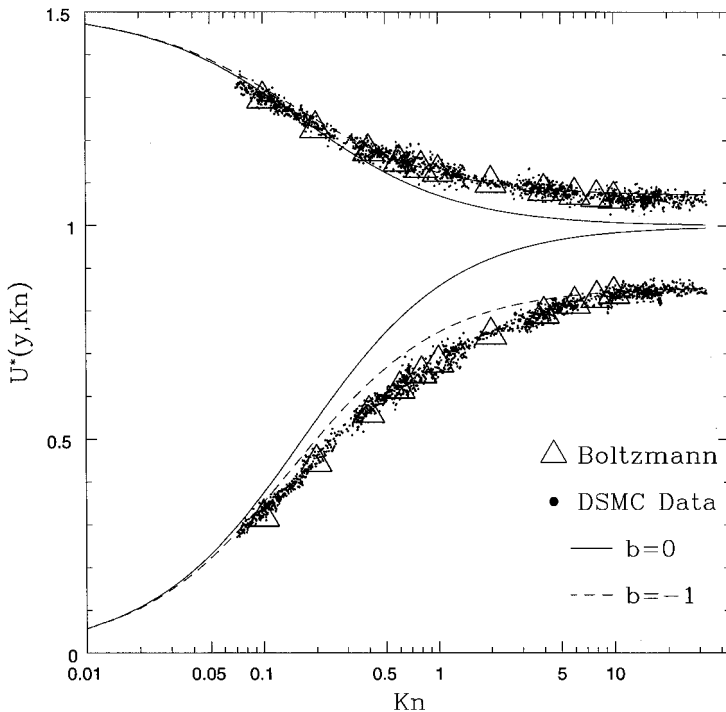
Figure 4. Velocity scaling at wall and centerline of the channels for slip and transition flows. The linearized Boltzmann solution of Ohwada et al. [23] is shown by triangles, the DSMC simulations are shown by points. Theoretical predictions of velocity scaling for different values of b are also shown.

(monatomic molecules). The differences between the nitrogen and helium simula-
tions are negligible and thus this velocity scaling is independent of the gas type.
The linearized Boltzmann solution of Ohwada et al. [23] for a monatomic gas is
also shown in Figure 4 by triangles. This solution closely matches the DSMC
predictions. Maxwell's first-order boundary condition ($b = 0$) (shown by solid line)
predicts erroneously a uniform nondimensional velocity profile for large Knudsen
number. The breakdown of *slip flow theory* based on the first-order slip boundary
conditions is realized around $Kn = 0.1$ and $Kn = 0.4$ for the wall and the center-
line velocity, respectively. This finding is consistent with commonly accepted limits
of the slip flow regime [10]. The prediction using $b = -1$ is shown by small-dashed
lines. The corresponding centerline velocity closely follows the DSMC results,
while the slip velocity of the model with $b = -1$ deviates from DSMC in the
intermediate range for $0.1 < Kn < 5$. One possible reason for this is the effect of
Knudsen layer: For small Kn flows the Knudsen layer is thin and does not affect
the slip velocity prediction too much. For very large Kn flows, the Knudsen layer
covers the channel entirely. However, for intermediate Kn values both the fully
developed viscous flow (boundary layer) and the Knudsen layer exist in the
channel. At this intermediate range, approximating the velocity profile to be
parabolic ignores the Knudsen layers. For this reason, the model with $b = -1$
results in 10% error of the slip velocity at $Kn = 1$. However, the velocity distribu-
tion in the rest of the channel is described accurately for the entire flow regime.

3.2.2 Flow rate scaling.

The volumetric flow rate in a channel is a
function of channel dimensions, fluid properties (μ_0, λ), and pressure drop, and it
can be written as

$$\dot{Q} = \mathscr{G}\left(\frac{dP}{dx}, \mu_0, h, \lambda\right)$$

For a channel of thickness h, using the Navier-Stokes solution and the general slip
boundary condition (12), we obtain

$$\dot{Q} = -\frac{h^3}{12\mu_0}\frac{dP}{dx}\left(1 + \frac{6\,Kn}{1 - b\,Kn}\right) \tag{15}$$

where $Kn = \lambda/h$.

The slip model (12) gives good agreement with DSMC data and the linearized
Boltzmann solutions for the *nondimensional velocity profile*, but does not predict
the flow rate correctly [39]. This is expected, as the Navier-Stokes equations are
invalid in this regime. In fact, the dynamic viscosity, which defines the diffusion of
momentum due to the intermolecular collisions, must be modified to account for
the increased rarefaction effects. The kinetic theory description for dynamic
viscosity requires $\mu_0 \simeq \lambda \bar{v} \rho$, where $\bar{v}$ is the mean thermal speed. Using mean free
path λ in this relation is valid as long as intermolecular collisions are the dominant
part of momentum transport in the fluid (i.e., $Kn \ll 1$). However, for increased
rarefaction, intermolecular collisions are reduced significantly and in the free
molecular flow regime only the collisions of the molecules with the walls should be

considered. Therefore, in free molecular channel flow the diffusion coefficient should be based on characteristic length scale h (channel height) as $\mu \simeq h\bar{v}\rho$ [46]. Since the diffusion coefficient is based on λ in the slip/continuum flow regime and h in the free molecular flow regime, we propose to model the variation of diffusion coefficient with the following formula:

$$\mu \simeq \rho\bar{v}\left[\frac{1}{(1/h) + (1/\lambda)}\right] = \rho\bar{v}\lambda\left[\frac{1}{1 + \text{Kn}}\right]$$

which can be simplified as

$$\mu(\text{Kn}) = \mu_0\left(\frac{1}{1 + \text{Kn}}\right) \tag{16}$$

where μ_0 is the dynamic viscosity of the gas at a specified temperature and μ is the generalized diffusion coefficient. The variable diffusion coefficient model presented above is based on a simple analysis. Another point of view is to consider the ratio of intermolecular collisions of the molecules (f_g) to the total number of collisions per unit time (i.e., sum of intermolecular and wall collisions $f_g + f_w$). Following [9], the frequency of wall collisions in a channel section is (with width w, height h, and length dx)

$$f_w = \frac{1}{4}n\bar{v}2(h + w)\,dx$$

The intermolecular collision frequency in the flow volume is

$$f_g = \frac{\bar{v}}{\lambda}nhw\,dx$$

where $\bar{v}$ is the mean thermal speed and n is the number density. Assuming that $w \gg h$, the ratio of intermolecular collisions to total collisions becomes

$$\frac{f_g}{f_g + f_w} = \frac{1}{1 + \frac{1}{2}\text{Kn}} \tag{17}$$

This analysis has resulted in a correction to the continuum-based flow rate models, similar to the variable diffusion coefficient model presented earlier, with the only difference of $\frac{1}{2}$ in front of the Kn term.

The increased rarefaction effects in our flow rate model can be taken into account by introducing a correction expressed as *rarefaction coefficient* $C_r(\text{Kn})$, which is a function of Knudsen number. The flow rate is then obtained as

$$\dot{Q} = -\frac{h^3}{12\mu}\frac{dP}{dx}\left(1 + \frac{6\,\text{Kn}}{1 - b\,\text{Kn}}\right) = -\frac{h^3}{12\mu_0}\frac{dP}{dx}\left(1 + \frac{6\,\text{Kn}}{1 - b\,\text{Kn}}\right)C_r(\text{Kn}) \tag{18}$$

where $C_r(\text{Kn})$ is a general function of Knudsen number. A possible model for C_r is suggested by the aforementioned analysis [Eqs. (16) and (17)] in the form $C_r(\text{Kn}) = 1 + \alpha\,\text{Kn}$. If we assume that α is a constant in the entire Knudsen regime, the enhanced flow rate in the slip flow regime will be given as

$$\frac{\dot{M}}{\dot{M}_C} = 1 + (6 + \alpha)\,\text{Kn} + \mathcal{O}(\text{Kn}^2)$$

where $\dot{M}_C$ corresponds to continuum mass flow rate. This model becomes inaccurate for a nonzero value of α in the slip flow regime. Moreover, in the free/molecular flow regime, for very long channels ($L \gg \lambda \gg h$) there are no physical values for α, since the flow rate increases logarithmically with Kn. For finite-length channels the flow rate asymptotes to a constant value proportional to $\log_e(L/h)$ (see Figure 2). Therefore, for finite-length two-dimensional channel flows, the coefficient α should vary smoothly from zero in the slip flow regime to an appropriate constant value in the free molecular flow regime. It is difficult to verify this variation using the DSMC simulations due to the statistical scatter of the DSMC method. However, progress can be made if we assume an approximate value of α, which we denote by $\bar{\alpha}$, and determine the value of it for a specific gas in a finite length channel. Such an analysis was performed in [39] for nitrogen flow in a channel of length-to-height ratio $L/h = 20$, resulting in $\bar{\alpha} = 2.2$.

Using this approximate value we compare the predictions of the model for mass flow rate versus DSMC results. By integrating Eq. (18) from the inlet to the exit of the channel, we derive an expression for the mass flow rate per unit width:

$$\dot{M} = \frac{h^3 P_0}{24\mu_0 RT_0}\frac{\Delta P}{L}\left[(\Pi + 1) + 2(6 + \bar{\alpha})\,\text{Kn}_0 \right.$$

$$\left. + \frac{12(b + \bar{\alpha})}{\Pi - 1}\,\text{Kn}_0^2\,\log_e\left(\frac{\Pi - b\,\text{Kn}_0}{1 - b\,\text{Kn}_0}\right)\right] \qquad (19)$$

where the subscript 0 refers to exit conditions, $\Pi = P_i/P_0$ (inlet-to-exit pressure ratio), and L is the channel length. The comparison of the corrected model with the DSMC data is given in Figure 5. The model predicts Knudsen's minimum obtained by the DSMC calculations quite accurately at $\text{Kn} \approx 1.0$. Consistent with the DSMC solutions, the model predicts a flow rate independent of Kn for the free molecular flow limit. However, this constant flow rate for larger Kn is slightly (13%) lower than the DSMC predictions. For comparisons with the model and the DSMC data, we also plot the flow rate obtained by the continuum and the first-order slip models in Figure 5. The continuum model behaves like $1/\text{Kn}$ and gives the wrong variation, while the slip flow model results in flow rate values three times less than the DSMC calculations.

The corresponding free molecular mass flow rate of the new model can be calculated using an asymptotic expansion of Eq. (19) in $1/\text{Kn}$ as $\text{Kn} \to \infty$. The result is independent of both the Knudsen number and the pressure ratio [since
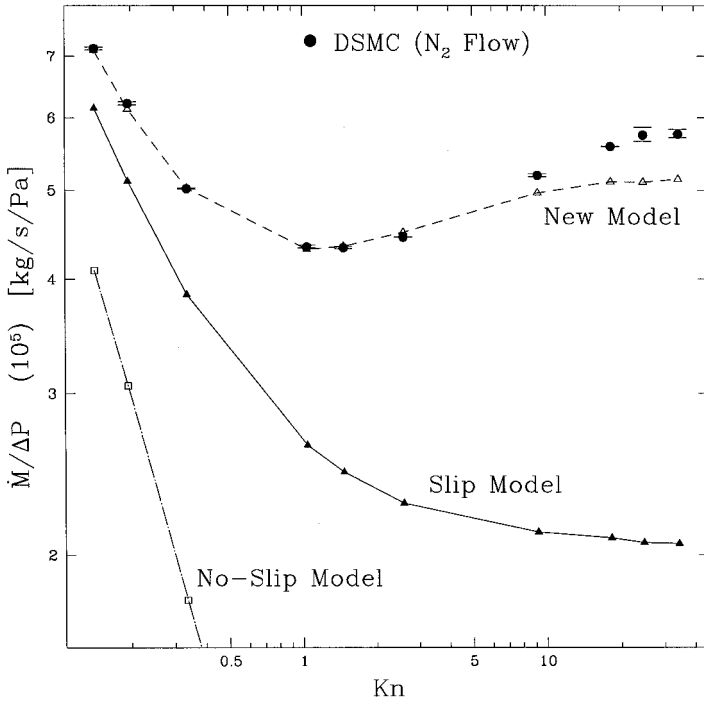
Figure 5. Variation of mass flow rate (per pressure drop ΔP) as a function of exit Knudsen number in the channel. Knudsen's minimum is captured by the model at $Kn \simeq 1$. Comparisons with the continuum and slip models are also included.

$Kn_0 \to \infty$, $(\Pi - 1)/(b\, Kn_0) \ll 1$], i.e.,

$$\dot{M}_{FM} = \frac{h^2}{12}\left(\frac{\pi}{2RT}\right)^{1/2}\frac{\Delta P}{L}\left[\overline{\alpha}\left(1 - \frac{6}{b}\right)\right] \qquad (20)$$

Having obtained the mass flow rate, the corresponding pressure distribution along the channel can be obtained as

$$\tilde{P}^2 - 1 + 2(6 + \overline{\alpha})\left(\frac{2 - \sigma_v}{\sigma_v}\right)Kn_0(\tilde{P} - 1)$$

$$+ 2(6b + \overline{\alpha})\left(\frac{2 - \sigma_v}{\sigma_v}\right)Kn_0^2 \log_e\left(\frac{\tilde{P} - b\,Kn_0}{1 - b\,Kn_0}\right) = B\left(1 - \frac{x}{L}\right) \qquad (21)$$

where B is a constant such that $\tilde{P}(0) = (P_i/P_0) = \Pi$. Here we have defined $\tilde{P}(x) = P(x)/P_0$, i.e., the pressure at a station x normalized with the exit pressure.

The above equation provides an implicit relation for $\tilde{P}$. The pressure distribution for a first-order boundary condition is obtained explicitly by neglecting the second-order terms $[\mathcal{O}(Kn^2)]$ in Eq. (22).

We also examine the differences in pressure between DSMC and μ**Flow** predictions by plotting the curvature in the pressure distribution [i.e., the deviation from the corresponding linear pressure drop $(P - P_{IC})/(P_0)$] in Figure 6, where P_{IC} denotes the pressure of corresponding incompressible flow. The μ**Flow** simulation [using the slip boundary condition of Eq. (5)] predicts larger curvature in pressure distribution than the DSMC results. The pressure distribution obtained by the first-order boundary condition is shown by dashed lines and lies between the μ**Flow** and DSMC results. Our second-order slip model without the correction of the rarefaction coefficient ($C_r = 1 + \bar{\alpha} \, Kn$) gives identical results to μ**Flow** predictions. The corresponding continuum (no-slip) pressure distribution is also given in the figure. The reduction in the curvature of the pressure distribution with rarefaction is clearly demonstrated. Finally, the model that includes the rarefaction coefficient $C_r(Kn)$ (shown by solid lines) gives results closest to the DSMC solution. This shows the ability of the new model in predicting the pressure distribution for channel flows. At higher Knudsen number, the curvature in the
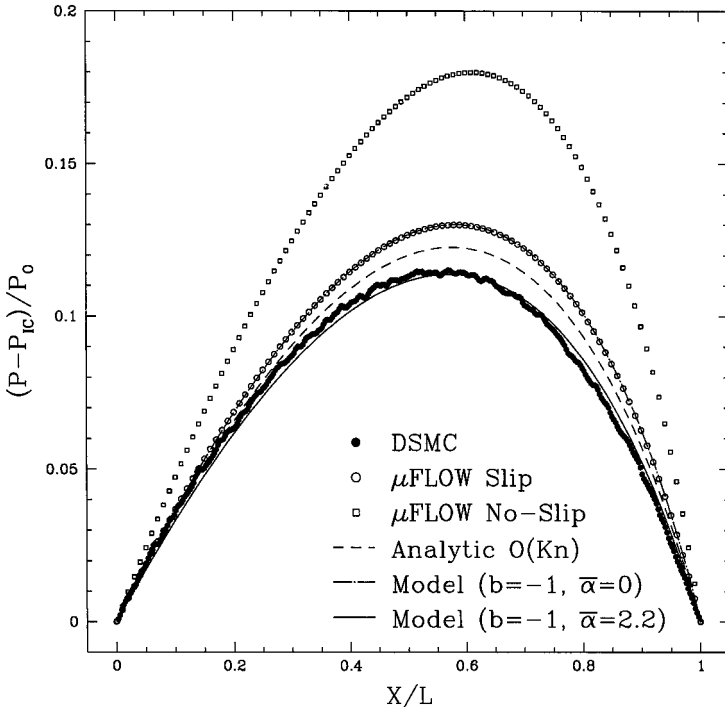
Figure 6. Deviations from linear pressure drop for nitrogen flow ($\Pi = 2.28$, $Kn_0 = 0.2$). Comparison of μ**Flow** with the DSMC predictions and the new slip model ($b = -1, \bar{\alpha} = 2.2$).

pressure distribution is much smaller, with linear pressure drop observed as $\mathrm{Kn} \to \infty$.

4 MODEL FOR PIPE AND DUCT FLOWS

The asymptotic value of flow rate for pipe and duct flows at high Knudsen number is constant, and this offers the possibility of obtaining a model for the rarefaction coefficient $C_r(\mathrm{Kn})$ and in particular the coefficient α. The objective is to construct a unified expression for $\alpha(\mathrm{Kn})$ which represents the transition of α from zero in the slip flow regime to its asymptotic constant value in the free molecular flow regime. We will verify the velocity and new flow rate models using available experimental data for pipes (S. Tison, NIST, private communications), as well as numerical results obtained in [24, 49] for pipe and duct flows, respectively.

First, we derive a similar model for the pipe flow. Assuming a parabolic velocity profile with the slip amount given by (12), it is possible to obtain the following equation:

$$U^*(r, \mathrm{Kn}) = \frac{U(x, r)}{\overline{U}(x)} = \left[\frac{-(r/a)^2 + 1 + 2\,\mathrm{Kn}/(1 - b\,\mathrm{Kn})}{(1/2) + 2\,\mathrm{Kn}/(1 - b\,\mathrm{Kn})} \right] \tag{22}$$
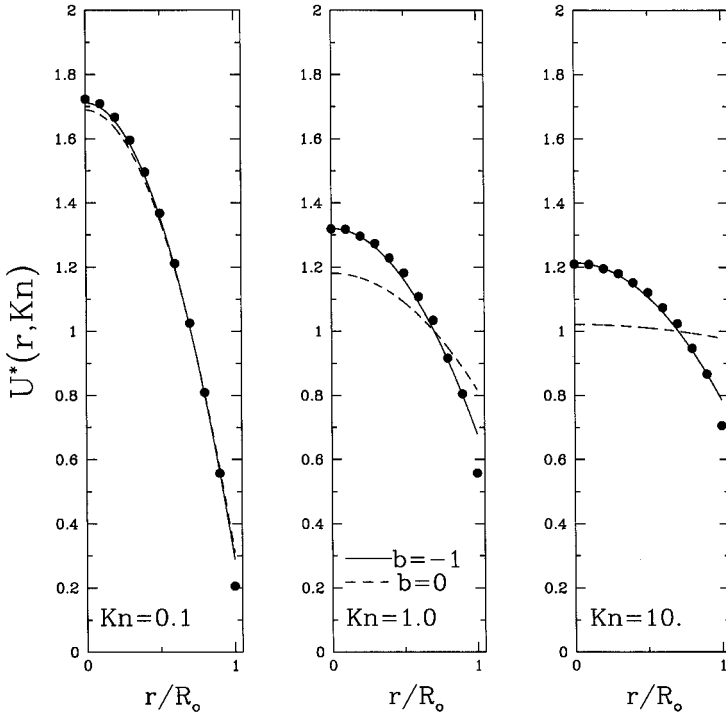
where a is the pipe radius, and the Knudsen number is defined as $\mathrm{Kn} = \lambda/a$. We compare the nondimensional velocity scaling with the linearized Boltzmann solution of [24] in Figure 7. The general slip coefficient is found to be $b = -1$ as before, consistent with the velocity profiles given in [24] for cases $\mathrm{Kn} = 0.1$, $\mathrm{Kn} = 1.0$, and $\mathrm{Kn} = 10$. The velocity profiles predicted with the first-order slip model and the general slip model of Eq. (12) are also shown in Figure 7. It is seen that the first-order model gives erroneous velocity distributions in the transitional and free molecular flow regime. For example, for the $\mathrm{Kn} = 10$ case an almost uniform velocity distribution is predicted. However, the model of Eq. (12) predicts accurately the velocity distribution in most of the pipe with a small error in the slip velocity.

Next, we compare the flow rate model corrected as before by the rarefaction coefficient $C_r(\mathrm{Kn})$ in a similar form obtained for channel flows $[C_r(\mathrm{Kn}) = 1 + \alpha\,\mathrm{Kn}]$. The volumetric flow rate for a pipe is

$$\dot{Q} = -\frac{\pi a^4}{8\mu_0} \frac{dP}{dx}(1 + \alpha\,\mathrm{Kn})\left(1 + \frac{4}{1 - b\,\mathrm{Kn}}\right) \tag{23}$$

and the corresponding mass flow rate is

$$\dot{M} = \frac{\pi a^4 P_0}{16\mu_0 RT_0} \frac{\Delta P}{L}\left[(\Pi + 1) + 2(4 + \alpha)\,\mathrm{Kn}_0\right.$$

$$\left. + \frac{8(\alpha + b)}{\Pi - 1}\,\mathrm{Kn}_0^2 \log_e\left(\frac{\Pi - b\,\mathrm{Kn}_0}{1 - b\,\mathrm{Kn}_0}\right)\right] \tag{24}$$

Figure 7. Nondimensional velocity profile scaling in rarefied pipe flows. The dots correspond to linearized Boltzmann solution of Loyalka and Hamoodi. The first-order model corresponds to $b = 0$, the general slip model corresponds to $b = -1$.

Since $b = -1$ is already determined from the linearized Boltzmann solution, the only parameter to be determined in the model is α. However, α should vary from zero in the slip flow regime to a constant asymptotic value (α_0) in the free molecular flow regime. It is possible to obtain the constant asymptotic value of α (as Kn $\to \infty$) by using the theoretical mass flow rate in the free molecular flow regime given by Eq. (13) and the asymptotic value for the mass flow rate obtained by (24) for Kn $\to \infty$, as

$$\alpha_{\text{Kn} \to \infty} \equiv \alpha_0 = \left[\frac{64}{3\pi (1 - 4/b)} \right] \tag{25}$$

We can also compare our results with the formula derived by Knudsen [50], which we normalize here with the corresponding free molecular flow limit (13).

$$\frac{\dot{M}_{\text{Kn}}}{\dot{M}_{\text{FM}}} = \frac{3\pi}{64 \overline{\text{Kn}}} + \left[\frac{1 + 2.507 (1/\overline{\text{Kn}})}{1 + 3.095 (1/\overline{\text{Kn}})} \right] \tag{26}$$

where $\overline{Kn}$ is computed at the average pressure $\overline{P} = (P_i + P_0)/2$. The constants 2.507 and 3.095 are taken from Loeb [51], where details of derivation of Knudsen's formula are presented. The same formula has also been used in [7] and [24].

Due to the lack of detailed experimental data, we do not have exact values for the pressure ratio Π and thus we cannot use Eq. (24) directly. Instead, we approximately integrate the volumetric flow rate equation (23) by multiplying it with the average density in order to obtain the mass flow rate. The flow conditions are evaluated at an average state. For example, the average pressure is defined as $\overline{P} = (P_i + P_0)/2$ so that $(dP/dx) = \Delta P/L$, and Kn is evaluated at $\overline{P}$. The corresponding mass flow rate becomes

$$\dot{M} = - \frac{\pi a^4 \overline{P}}{8\mu_0 RT} \frac{\Delta P}{L}(1 + \alpha\,Kn)\left(1 + \frac{4\,Kn}{1 - b\,Kn}\right) \tag{27}$$

Nondimensionalizing this relation with the theoretical free molecular flow limit (13), we obtain the following relation:

$$\frac{\dot{M}}{\dot{M}_{FM}} = \frac{3\pi}{64\,Kn}(1 + \alpha\,\overline{Kn})\left(1 + \frac{4\,\overline{Kn}}{1 - b\,\overline{Kn}}\right) \tag{28}$$

Comparison of (26) and (28) shows both models predict the same limit in the free molecular flow regime (Kn $\rightarrow \infty$) if the value of α_0 is chosen according to Eq. (25) ($\alpha_0 = 1.358$ for pipe flows, i.e., $\alpha \ll \lambda \ll L$).

Knudsen's formula is often used to describe the flow for the entire flow regime, including the slip flow regime. Considering that $\dot{M}_C/\dot{M}_{FM} = 3\pi/64\,\overline{Kn}$, Knudsen's formula can be written for the slip flow regime (Kn $\leqslant 0.1$) as

$$\frac{\dot{M}_{Kn}}{\dot{M}_C} = 1 + \frac{64\,\overline{Kn}}{3\pi}\left(\frac{2.507}{3.095}\right) + \mathcal{O}(Kn^2)$$

where the subscript C stands for *continuum* predictions. This relation shows that Knudsen's formula is not accurate for the slip flow regime, as the first-order variation of flow rate from the corresponding continuum limit should be

$$\frac{\dot{M}_{slip}}{\dot{M}_C} = 1 + 4\,\overline{Kn}$$

If we used a constant α in the entire flow regime, our model would have resulted in an undesired form, similar to Knudsen's model in the slip flow regime. In order to obtain the variation of α as a function of Knudsen number for the transitional flow regime, we can solve for α from Eq. (28) as

$$\alpha = \frac{64\left(\dot{M}/\dot{M}_{FM}\right)}{3\pi\left[1 + 4\,\overline{Kn}/(1 - b\,\overline{Kn})\right]} - \frac{1}{Kn}$$

where $\dot{M}$ is the flow rate data obtained numerically or experimentally (and normalized with $\dot{M}_{FM}$). The $1/Kn$ behavior in this analytical expression makes it difficult to predict the value of α for small Kn. Therefore, we must rely on accurate numerical or experimental data. For this purpose we use the linearized Boltzmann solution of [24] and experimental data of S. Tison (NIST, private communications). In Figure 8 we present the variation of α as a function of Kn (symbols). The value of α is initially small (close to zero), and it gradually increases with Kn, reaching a constant value in the free molecular flow regime. The physical meaning of this behavior is that the dynamic viscosity remains the standard diffusion coefficient in the early slip flow regime. The value of α increases slowly with Kn in the slip flow regime, and therefore the effect of change of the diffusion coefficient is second-order in Kn. For this reason, the experimental slip flow results are accurately predicted by the slip flow theory, which does not require change of the diffusion coefficient length scale from λ to channel height h. The variation of α as a function of Kn obtained by the numerical and experimental data can be represented accurately with the following relation:

$$\alpha = \alpha_0 \frac{2}{\pi} \tan^{-1}\left(\alpha_1 \overline{Kn}^{\beta}\right) \tag{29}$$
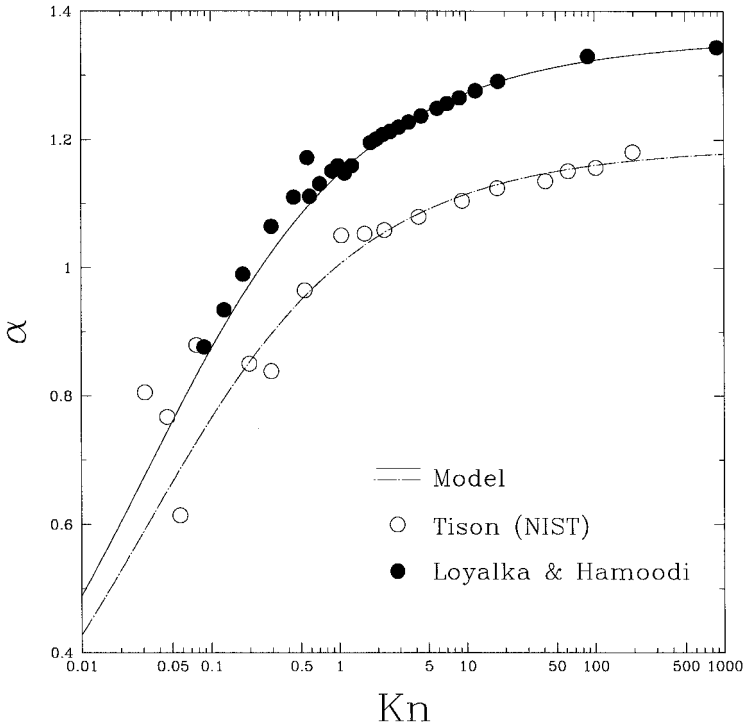
Figure 8. Variation of α as a function of Knudsen number. Analytical fit to this variation is obtained by $\alpha = \alpha_0 (2/\pi) \tan^{-1}(\alpha_1 Kn^{\beta})(\alpha_1$ and β are free parameters).

where α_0 is determined to result in the desired free molecular flow rate using (25) and $\alpha_1 = 4.0$, $\beta = 0.4$. This model is shown in Figure 8 with lines. Note that the values for α_1 and β are the same for both the experimental and numerical results presented in the figure, and that these are the only two undetermined parameters of the model.

In Figure 9 we present the flow rate variation as a function of Kn. The data is obtained by the solution of linearized Boltzmann equations by Loyalka and Hamoodi [24] for a very long channel (so that $h \ll \lambda \ll L$ is maintained for any value of Kn). Knudsen's two-parameter model is also presented. Experimental data presented in the figure is obtained by Tison for helium flow in finite-length tubes ($L/a = 200$). There are differences between the experimental and numerical data. For example, the experimental data has not reached the corresponding free molecular flow rate limit. At Kn $= 200$ (highest Kn data in the experiments) $L \approx \lambda$, and therefore end effects are important and the expected mass flow rate is less than the theoretical free molecular flow rate [46]. Since the analytical and experimental data show some differences, in the case of the experiments we found the value of $\alpha_0 = 1.19$ by using the experimental data at Kn $= 200$. Also, for the linearized Boltzmann solution we obtained $\alpha_0 = 1.358$ using Eq. (25). Our model's
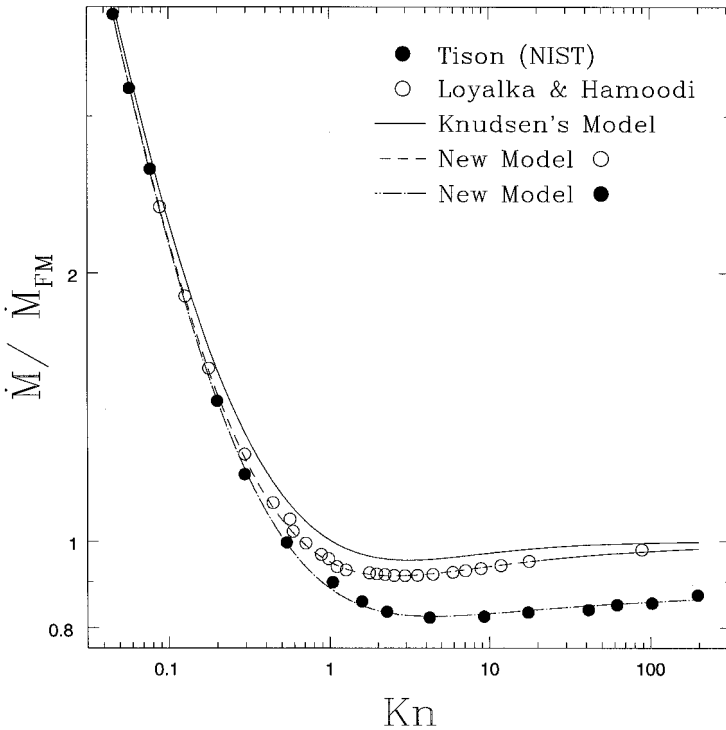
Figure 9. Free molecular scaling of Loyalka and Hamoodi's linearized Boltzmann solutions and Tison's experiments. Comparisons with the proposed model for both cases and Knudsen's model are also presented.

predictions for the linearized Boltzmann solution and experimental data are also presented in the figure. The model describes the variation of the data very accurately, and it is successful in predicting the Knudsen's minimum.

In Figure 10 we present the mass flow rate variation (normalized with the corresponding continuum value) as a function of Kn up to Kn = 0.5. This covers the slip and the early transitional flow regime. We see that Knudsen's model is not accurate in this regime. Linearized Boltzmann solutions and experimental data both start with slope of 4 [i.e., $\dot{M}/\dot{M}_C = 1 + 4\,\mathrm{Kn} + \mathcal{O}(\mathrm{Kn}^2)$], then the slope increases gradually with Kn. Our model predicts this transition very accurately for the numerical and the experimental data. The increase in slope was observed by Sreekanth [13] and explained as a change in the slip coefficient in Maxwell's slip boundary conditions from 1.0 to 1.1466. If the change in the slope of the data is to be explained by an increase in the slip coefficient, the velocity scaling results shown in Figure 7 and Figure 3 should be affected. It is clearly seen that such an effect is not present, and therefore a more appropriate explanation of the slope change is the *change* in the diffusion coefficient with Kn as presented above.
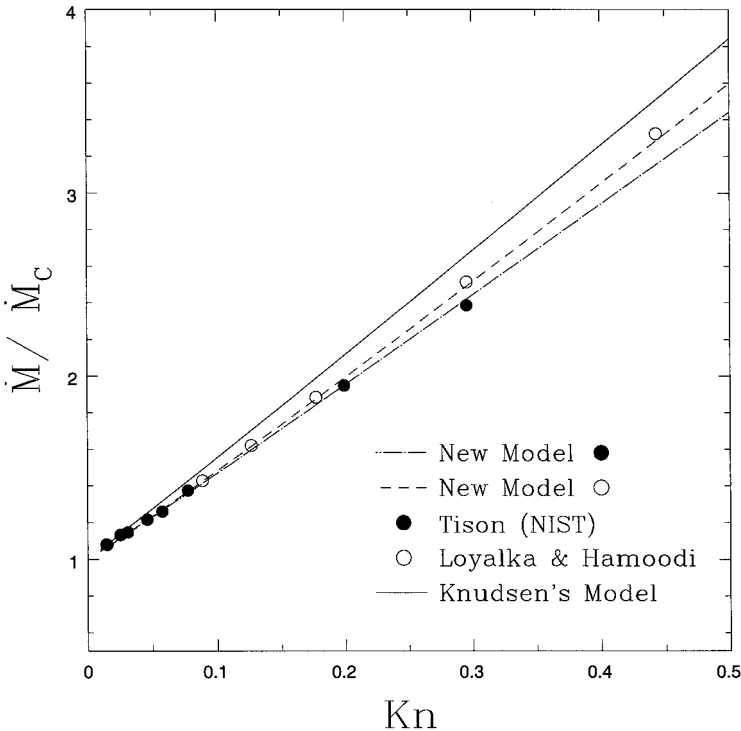
Figure 10. Normalized flow rate variation in the slip and early transitional flow regimes for pipe flows. Symbols correspond to the linearized Boltzmann solutions of Loyalka and Hamoodi [24] and experimental results by Tison. Comparisons with the proposed model for both cases and Knudsen's model are also presented.

Finally, we present the extensions of our model for duct flows in the entire flow regime. We consider flows in ducts with aspect ratios (AR $= w/h \equiv$ width/height) of 1, 2, and 4. The data are obtained by linearized Boltzmann solution in ducts with the corresponding aspect ratios [49]. Our previous analysis was valid for two-dimensional channels, where we reported flow rate per channel width. For duct flows, three-dimensionality of the flow field (due to the side walls of the duct) must be considered. In continuum duct flows the flow rate formula developed for two-dimensional channel flows is corrected in order to include the blockage effects of the side walls. Correspondingly, the volumetric flow rate in a duct with aspect ratio (AR) for continuum flows is (see [52], p. 120)

$$\dot{Q} = C(\text{AR}) \frac{wh^3}{12\mu} \left(-\frac{dP}{dx} \right)$$

where $C(\text{AR})$ is the correction factor given as

$$C(\text{AR}) = \left\{ 1 - \frac{192(\text{AR})}{\pi^5} \sum_{i=1,3,5,\ldots}^{\infty} \frac{\tanh[i\pi/2(\text{AR})]}{i^5} \right\} \tag{30}$$

With this correction, aspect ratio 1, 2, and 4 ducts correspond to 42.17%, 68.60%, and 84.24% of the theoretical two-dimensional channel volumetric flow rate for continuum flows, respectively. According to our model, the volumetric flow rate for rarefied gas flows in ducts should be given by

$$\dot{Q} = C(\text{AR}) \frac{wh^3}{12\mu_0} \left(-\frac{dP}{dx} \right)(1 + \alpha \, \text{Kn})\left(1 + \frac{6 \, \text{Kn}}{1 - b \, \text{Kn}} \right)$$

where the correction factor $C(\text{AR})$ is independent of Knudsen number. The variation of α as a function of Kn is calculated by using the correction factors [$C(\text{AR})$], the linearized Boltzmann solutions in [49], and our model. This variation is given in Figure 11. The rarefaction coefficient [$C_r(\text{Kn}) = 1 + \alpha \, \text{Kn}$] was introduced in order to model the reductions in the intermolecular collisions of the molecules as the Kn is increased. In duct flows both the height and the width of the duct are important length scales, and comparison of these length scales to the local mean free path is an important factor in the variation of α. It is seen in Figure 11 that the transition in α occurs later for high-aspect-ratio ducts, as expected.

Similar to the pipe flow case, an approximate analytical formula can be derived to describe the mass flow rate in ducts of various aspect ratios as

$$\frac{\dot{M}}{\dot{M}_C} = C(\text{AR})(1 + \alpha \overline{\text{Kn}})\left(1 + \frac{6 \, \overline{\text{Kn}}}{1 - b \, \overline{\text{Kn}}} \right)$$

where the $\overline{\text{Kn}}$ is evaluated at average pressure as before. In Figure 12 we present the variation of flow rate nondimensionalized with the corresponding continuum value as a function of Kn in the slip and early transitional flow regime. The linear
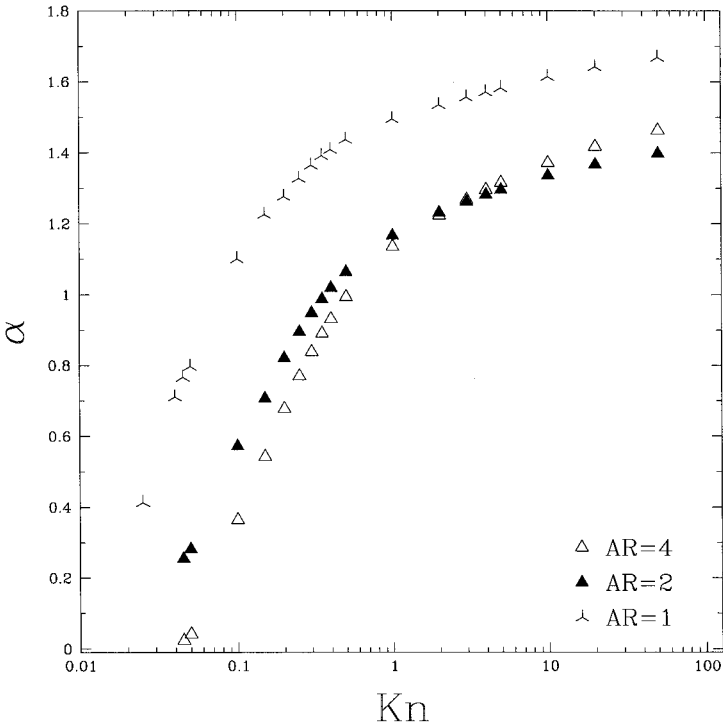
Figure 11. Variation of α as a function of Kn for various aspect-ratio ducts.

increase of the flow rate with Kn, and complete description of rarefied duct flows with the introduction of the correction factor $C(AR)$, is observed. The slope of the nondimensionalized mass flow rate increases gradually with Kn. This is attributed to the gradual change in the rarefaction coefficient as presented in Figure 11.

For the free molecular scaling of the data, we nondimensionalized the flow rate with

$$\dot{M}_{FM} = \frac{h^2 w}{\sqrt{2RT_0}} \frac{\Delta P}{L}$$

which gives the correct order of magnitude for the flow rate. The exact value of the free molecular flow rate in rectangular ducts is given by [9]:

$$\dot{M}_{FM}(h, w) = \Gamma \dot{M}_{FM}$$

$$\Gamma = \left\{ h^2 w \log_e \left[\frac{h}{w} + \sqrt{1 + \left(\frac{h}{w}\right)^2} \right] + w^2 h \log_e \left[\frac{w}{h} + \sqrt{1 + \left(\frac{w}{h}\right)^2} \right] \right. \tag{31}$$

$$\left. - \frac{(h^2 + w^2)^{3/2}}{3} + \frac{h^3 + w^3}{3} \right\}$$
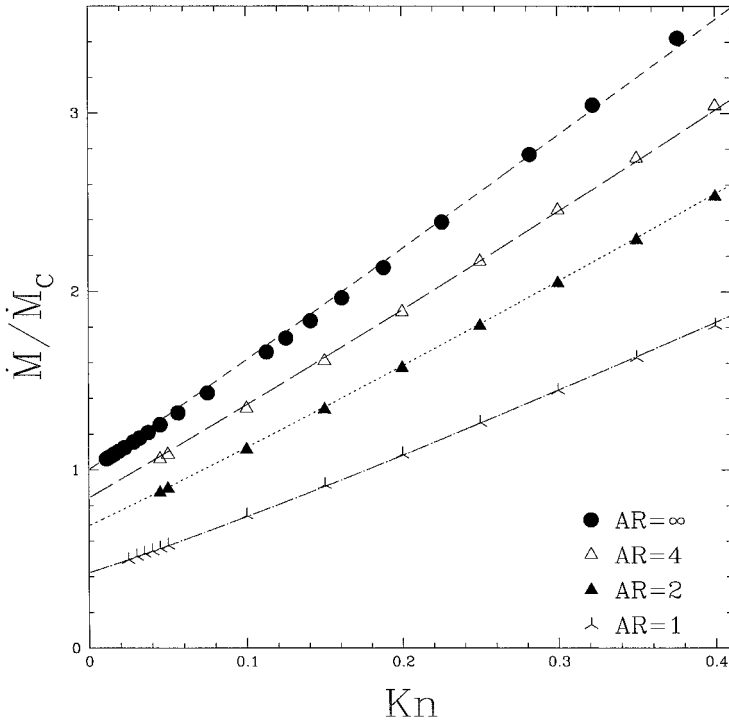
Figure 12. Normalized flow rate variation in the slip and early transitional flow regimes for various aspect-ratio (AR) duct flows. Symbols are the linearized Boltzmann solution of Sone and Hasegawa [49]. Comparisons with the proposed model are also presented by lines.

where h and w denotes the height and the width of the rectangular duct. For the aspect ratios (AR) of 1, 2, and 4 the above relation results in 0.8387, 1.1525, and 1.5008 $\dot{M}_{FM}$, respectively.

Nondimensionalizing our model with the free molecular mass flow rate ($\dot{M}_{FM}$), we obtain

$$\frac{\dot{M}}{\dot{M}_F} = \frac{C(AR)}{6\,\overline{Kn}}\left(1 + \alpha\,\overline{Kn}\right)\left(1 + \frac{6\,\overline{Kn}}{1 - b\,\overline{Kn}}\right)$$

In Figure 13 we present the variation of the nondimensionalized flow rate as a function of Kn. The duct flow data is due to Sone and Hasegawa [49], and the two-dimensional channel data (shown by AR = ∞) is due to Sone (for Kn ⩽ 0.17) and Cercignani (Kn > 0.17) [53]. Comparisons are made against the linearized Boltzmann solutions. For duct flows, good agreement of the model with the numerical data in the entire flow regime is obtained. The model is also able to capture Knudsen's minimum accurately. The parameters used in the model are given in Table 1. Note that α_0 is determined from the asymptotic constant limit of flow rate (31) Kn → ∞.
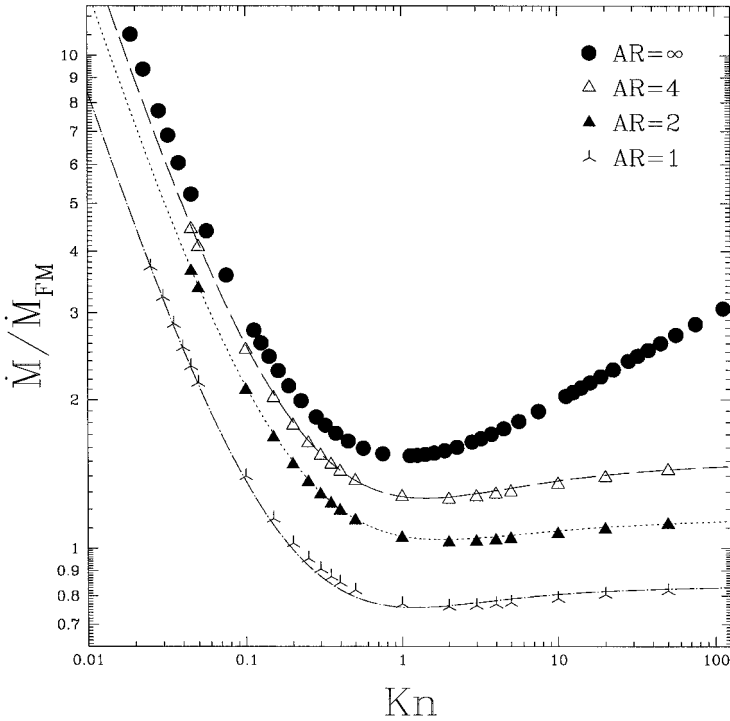
Figure 13. Free molecular scaling of Sone and Hasegawa's linearized Boltzmann solutions for duct flows of various aspect ratio. Comparisons with the proposed model are also presented by lines.

5 SUMMARY AND DISCUSSION

In this article we have developed a simple physics-based *unified model* that predicts the velocity distribution, the volumetric and mass flow rates, as well as the pressure distribution in channel, pipe, and duct flows (of general aspect ratio) for the entire flow regime (i.e., $0 \leqslant Kn < \infty$). This new model is a two-parameter model and it is able to predict Knudsen's minimum that occurs in the transitional flow regime. We compared our model against Knudsen's two-parameter model, which is valid strictly for pipe flows and can only predict flow rate. Knudsen's model overpredicts the flow rate in the slip flow regime, and it does not provide any information for the velocity or pressure distribution.

Table 1. Parameters of the model for various aspect-ratio duct flows. The only free parameters are α_1 and β, as α_0 can be determined from the asymptotic constant limit of flow rate as $Kn \to \infty$

$(AR) = w/h$	$C(AR)$	α_0	α_1	β
1	0.42173	1.7042	8.0	0.5
2	0.68605	1.4400	3.5	0.5
4	0.84244	1.5272	2.5	0.5

The proposed model is based on a general slip boundary condition [Eq. (12)], which is used to represent the velocity distribution in channels and pipes for the entire flow regime with reasonable accuracy. Modeling the velocity distribution as parabolic is a good approximation in the continuum, slip, and free molecular flow regimes. However, in the transition flow regime the model gives small deviations in the predictions of slip velocity. This deviation is due to growth of the Knudsen layer within the channel. A more accurate description of the velocity profile should include this sublayer in the approximation. This requires an analytic description of macroscopic flow properties in the Knudsen layer, which is currently not available. Neglecting the Knudsen layer results to a maximum 10% error in the slip velocity prediction at $Kn = 1.0$. However, the overall description of the velocity profile for the rest of the channel is still accurate. Our general slip boundary condition depends on the general slip coefficient b. For channel, duct, and pipe flows we have determined that $b = -1$. This choice of b corresponds to a second-order slip boundary condition in the slip flow regime. We have compared our model against DSMC simulations for monatomic and diatomic gas molecules and linearized Boltzmann solution for monatomic molecules. It has been observed that the universal velocity scaling and the value of b is unaffected by the gas type.

Flow rate modeling is based on the introduction of rarefaction coefficient in the form $C_r(Kn) = 1 + \alpha\,Kn$. The rarefaction coefficient models the effect of reduced intermolecular collisions with increased Kn. The value of α in this relation is determined by using the free molecular flow limit (α_0). However, the coefficient α is required to be zero in-order to capture the slip flow regime accurately. Therefore, α changes between zero in the slip, and a corresponding constant value (α_0) for the free molecular flow regimes. The experimental and numerical data have supported this observation. We have calculated the variation of α based on our model, and we have described this variation in the following form: $\alpha = \alpha_0 2/\pi \tan^{-1}(\alpha_1\,Kn^{\beta})$. This form introduced two new parameters into our model, α_1 and β, which are the *two free parameters* in the model. They describe the change of the slope of the normalized mass flow rate from the theoretical slip flow value in the early transitional flow regime ($Kn > 0.1$), and these two parameters should be determined by comparisons with experimental or numerical data.

We have also shown that the new model is able to predict the nonlinear pressure distribution in channels by comparisons against the DSMC data in the slip/early transitional flow regimes. For increased rarefaction effects the curvature in pressure distribution decreases and the pressure distribution becomes almost linear. This is true for pipe, duct, and channel flows in the free, molecular flow regime, where the flow rate is independent of density.

All of the simulations performed in this study are based on diffuse reflection (i.e., accommodation coefficient $\sigma_v = 1$). Therefore, in this study we did not validate the variation of slip conditions and velocity scaling as a function of the accommodation coefficient. In the future, studies of the unified model for nondiffuse (i.e., $\sigma < 1$) reflection cases should be performed. Since the velocity slip amount is affected directly by the accommodation coefficient, nondiffuse reflection cases can affect the mass and volumetric flow rate results significantly. Preliminary experimental results for silicon microchannels [19, 54] indicate tangential momen-

tum accommodation coefficient $\sigma_v \simeq 0.8$, due to the relatively small surface roughness obtained by microfabrication techniques.

REFERENCES

1. E. P. Muntz, Rarefied Gas Dynamics, *Annu. Rev. Fluid Mech.*, vol. 21, pp. 387–417, 1989.
2. S. A. Tison and C. R. Tilford, Low Density Water Vapor Measurements; the NIST Primary Standard and Instrument Response, NIST Internal Rep. 5241, 1993.
3. K. Gabriel, J. Jarvis, and W. Trimmer, Small Machines, Large Opportunities, NSF Tech. Rep., 1988.
4. N. Tagawa, State of the Art for Flying Head Slider Mechanisms in Magnetic Recording Disk, *Wear*, vol. 168, p. 43, 1993.
5. S. Fukui and R. Kaneko, Analysis of Ultra Thin Gas Film Lubrication Based on Linearized Boltzmann Equation: First Report—Derivation of a Generalized Lubrication Equation Including Thermal Creep Flow, *J. Tribol.*, vol. 110, pp. 253–262, 1988.
6. F. J. Alexander, A. L. Garcia, and B. J. Alder, Direct Simulation Monte Carlo for Thin-Film Bearings, *Phys. Fluids*, vol. 6, no. 12, pp. 3854–3860, 1994.
7. S. A. Tison, Experimental Data and Theoretical Modeling of Gas Flows through Metal Capillary Leaks, *Vacuum*, vol. 44, pp. 1171–1175, 1993.
8. D. G. Coronell and K. F. Jensen, Analysis of Transition Regime Flows in Low Pressure CVD Reactors Using the Direct Simulation Monte Carlo Method, *J. Electrochem. Soc.*, vol. 139, pp. 2264–2273, 1992.
9. S. L. Thompson and W. R. Owens, A Survey of Flow at Low Pressures, *Vacuum*, vol. 25, pp. 151–156, 1975.
10. S. A. Schaaf and P. L. Chambre, *Flow of Rarefied Gases*, Princeton University Press, Princeton, NJ, 1961.
11. A. Beskok, W. Trimmer, and G. E. Karniadakis, Rarefaction and Compressibility Effects in Gas Microflows, *J. Fluids Eng.*, vol. 118, no. 3, pp. 448–456, 1996.
12. A. Beskok, W. Trimmer, and G. E. Karniadakis, Rarefaction and Compressibility and Thermal Creep Effects in Gas Microflows, *IMECE 95, Proc. ASME Dynamic Systems and Control Division*, DSC-Vol. 57-2, pp. 877–892, 1995.
13. A. K. Sreekanth, Slip Flow through Long Circular Tubes, in L. Trilling and H. Y. Wachman (eds.), *Proc. Sixth Int. Symp. on Rarefied Gas Dynamics*, vol. 1, pp. 667–680, 1969.
14. J. Q. Liu, Y. C. Tai, K. C. Pong, and C. M. Ho, Micromachined Channel/Pressure Sensor Systems for Micro Flow Studies, *7th Int. Conf. on Solid-State Sensors and Actuators*, pp. 995–998, Transducers '93.
15. K. C. Pong, C. M. Ho, J. Liu, and Y. C. Tai, Non-linear Pressure Distribution in Uniform Microchannels, *Application of Microfabrication to Fluid Mechanics*, FED-Vol. 197, pp. 51–56, ASME, New York, 1994.
16. W. Gaede, Die äubere Reibung der Gase, *Annalen der Physik*, vol. 41, p. 289, 1913.
17. J. Pfahler, J. Harley, H. Bau, and J. Zemel, Gas and Liquid Flow in Small Channels, Symp. Micromechanical Sensors, Actuators, and Systems (ed. D. Cho, R. Warrington, Jr., A. Pisano, H. Bow, C. Friedrich, T. Tara-Almonte and J. Liburdy) ASME DSC, vol. 32, pp. 49–59, 1991.
18. J. C. Harley, Y. Huang, H. H. Bau, and J. N. Zemel, Gas Flow in Micro-channels, *J. Fluid Mech.*, vol. 284, pp. 257–274, 1995.
19. E. Arkilic, K. S. Breuer, and M. A. Schmidt, Gaseous Flow in Microchannels, *Application of Microfabrication to Fluid Mechanics*, FED-Vol. 197, pp. 57–66, ASME, New York, 1994.

20. A. Beskok and G. E. Karniadakis, Simulation of Slip-Flows in Complex Micro-geome-tries, *ASME DSC-Vol. 40*, pp. 355–370, 1992.

21. A. Beskok and G. E. Karniadakis, Simulation of Heat and Momentum Transfer in Complex Microgeometries, *AIAA J. Thermophys. Heat Transfer*, vol. 8, no. 4, pp. 647–655, 1994.

22. G. Bird, *Molecular Gas Dynamics and the Direct Simulation of Gas Flows*. Clarenton Press, Oxford, 1994.

23. T. Ohwada, Y. Sone, and K. Aoki, Numerical Analysis of the Poiseuille and Thermal Transpiration Flows between Two Parallel Plates on the Basis of the Boltzmann Equation for Hard Sphere Molecules, *Phys. Fluids A*, vol. 1, no. 12, pp. 2042–2049, 1989.

24. S. K. Loyalka and S. A. Hamoodi, Poiseuille Flow of a Rarefied Gas in a Cylindrical Tube: Solution of Linearized Boltzmann Equation, *Phys. Fluids A*, vol. 2, no. 11, pp. 2061–2065, 1990.

25. E. H. Kennard, *Kinetic Theory of Gasses*, McGraw-Hill, New York, 1938.

26. L. C. Woods, *An Introduction to the Kinetic Theory of Gases and Magnetoplasmas*, Oxford Science Publications, 1993.

27. S. Chapman and T. G. Cowling, *The Mathematical Theory of Non-uniform Gases*. Cambridge University Press, 1970.

28 C. Cercignani and A. Daneri, Flow of a Rarefied Gas between Two Parallel Plates, *J. Appl. Phys.*, vol. 34, pp. 3509–3513, 1963.

29. P. L. Bhatnagar, E. P. Gross, and K. Krook, A Model for Collision Processes in Gasses, *Phys. Rev.*, vol. 94, pp. 511–524, 1954.

30. A. B. Huang, D. P. Giddens, and C. W. Bagnal, Rarefied Gas Flow between Parallel Plates Based on the Discrete Ordinate Method, *Phys. Fluids*, vol. 10, no. 3, pp. 498–502, 1966.

31. K. Aoki, Numerical Analysis of Rarefied Gas Flows by Finite-Difference Method, in E. P. Muntz, D. P. Weaver, and D. H. Campbell, *Rarefied Gas Dynamics: Theoretical and Computational Techniques*, pp. 297–322, 1989.

32. W. Wagner, A Convergence Proof for Bird's Direct Simulation Monte Carlo Method for the Boltzmann Equation, *J. Stat. Phys.*, vol. 66, p. 1011, 1992.

33. G. Chen and I. D. Boyd, Statistical Error Analysis for the Direct Simulation Monte Carlo Technique, in *AIAA Fluid Dynamics Conference, June 19–22, 1995, San Diago, CA*, AIAA 95-2316.

34. F. J. Alexander, A. L. Garcia, and B. J. Alder, A Consistent Boltzmann Algorithm, *Phys. Rev. Lett.*, vol. 74, no. 26, pp. 5212–5215, 1995.

35. C. K. Oh, E. S. Oran, and B. Z. Cybyk, Microchannel Flow Computed with the DSMC-MLG, in *30th AIAA Thermophysics Conf., June 19–22, 1995, San Diego, CA*, AIAA 95-2090.

36. S. Y. Chou and D. Baganoff, Kinetic Flux-Vector Splitting for the Navier-Stokes Equations, Journal of Computational Physics, vol. 130, pp. 217–230, (1997).

37. M. Seidel and E. Steinheil, Measurement of Momentum Accomodations Coefficients on Surfaces Characterized by Auger Spectroscopy, SIMS and LEED, *Proc. 9th Int. Symp. on Rarefied Gas Dynamics*, pp. E9.1–E9.2, 1974.

38. R. G. Lord, Tangential Momentum Coefficients of Rare Gases on Polycrystalline Surfaces, *Proc. 10th Int. Symp. on Rarefied Gas Dynamics*, pp. 531–538, 1976.

39. A. Beskok, Simulations and Models for Gas Flows in Microgeometrics, Ph.D. thesis, Princeton University, Princeton, NJ, June 1996.

40. X. Zhong, On Numerical Solutions of Burnett Equations for Hypersonic Flow past 2-D Circular Blunt Leading edges in Continuum Transition Regime, *AIAA 42. Fluid Dynam-ics Conf., July 6–9, 1998, Orlando FL*, AIAA 93-3092.

41. R. Schamberg, The Fundamental Differential Equations and the Boundary Conditions for High Speed Slip-Flow, and Their Application to Several Specific Problems, Ph.D thesis, California Institute of Technology, Pasadena, CA, 1947.

42. R. G. Deissler, An Analysis of Second-Order Slip Flow and Temperature Jump Boundary Conditions for Rarefied Gases, *Int. J. Heat Mass Transfer*, vol. 7, pp. 681–694, 1964.

43. E. S. Piekos and K. S. Breuer, DSMC Modeling of Micromechanical Devices, *AIAA Thermophysics Conf., June 19–22, 1995, San Diego, CA*, AIAA 95-2089.

44. A. Beskok, Simulation of Heat and Momentum Transfer in Complex Micro-Geometries, Master's thesis, Princeton University, Princeton, NJ, June 1994.

45. C. Cercignani, Plane Poiseuille Flow and Knudsen Minimum Effect, in J. A. Laurmann (ed.), *Proc. Third Int. Symp. on Rarefied Gas Dynamics*, vol. 1, pp. 92–101, 1963.

46. W. G. Polard and R. D. Present, On Gaseous Self-diffusion in Long Capillary Tubes, *Phys. Rev.*, vol. 73, no. 7, pp. 762–774, 1948.

47. M. N. Kogan, *Rarefied Gas Dynamics*, Plenum Press, New York, 1969.

48. A. B. Huang and R. L. Stoy, Jr., Rarefied Gas Channel Flow for Three Molecular Models, *Phys. Fluids*, vol. 9, no. 12, pp. 2327–2336, 1966.

49. Y. Sone and M. Hasegawa, Poiseuille and Thermal Transpiration Flows of Rarefied Gas through a Rectangular Pipe (in Japanese), *J. Vacuum Soc. Jpn.*, vol. 30, no. 5, pp. 425–428, 1987.

50. M. Knudsen, Die Gesetze der Molekularströmung und der inneren Riebungsströmung der Gase durch Röhnen, *Annalen der Physik*, vol. 28, pp. 75–130, 1909.

51. L. B. Loeb, *Kinetic Theory of Gases*, Dover, New York, 1961.

52. F. M. White, *Viscous Fluid Flow*, McGraw-Hill International Editions, Mechanical Engineering Series, 1991.

53. S. Fukui and R. Kaneko, A Database for Interpolation of Poiseuille Flow Rates for High Knudsen Number Lubrication Problems, *J. Tribol.*, vol. 112, pp. 78–83, 1990.

54. E. Arkilic and K. S. Breuer, Gaseous Flow in Small Channels, in *AIAA Shear Flow Conf., July 6–9, 1992, Orlando, FL*; also *J. MicroElectro Mechanical Systems*, vol. 6, June 1997, AIAA 93-3270.

APPENDIX: BURNETT X–Y MOMENTUM EQUATION

Burnett X-momentum equation in a long channel ($\varepsilon = h/L$) including $\mathcal{O}(\varepsilon)$ terms:

$$
P_x\left[1 - \left(\frac{\omega_2}{3} + \frac{\omega_6}{12}\right)\frac{\gamma\pi}{2}\,\mathrm{Kn}_0^2\,M_0^2\left(\frac{p_0^2}{p}\right)(U_y)^2\right]
$$

$$
= U_{yy} + \varepsilon\left\{\sqrt{\frac{\gamma\pi}{2}}\,M_0\,\mathrm{Kn}_0\left(\frac{p_0}{p}\right)\left[\left(\frac{\omega_1}{2} - \frac{7\omega_2}{3} + \frac{\omega_6}{3}\right)U_y U_{yx}\right.\right.
$$

$$
\left.\left. + \left(\frac{\omega_1}{2} - \frac{7\omega_2}{2} + \frac{\omega_6}{6}\right)U_x U_{yy}\right]\right\}
$$

$$
+ \varepsilon\left\{\sqrt{\frac{\gamma\pi}{2}}\,M_0\,\mathrm{Kn}_0\left(\frac{p_0}{p}\right)\left[\left(\frac{\omega_1}{2} - \frac{\omega_2}{6} + \frac{\omega_6}{6}\right)U_y V_{yy}\right.\right.
$$

$$
\left.\left. + \left(\frac{\omega_1}{2} + \frac{\omega_2}{2} + \frac{\omega_6}{6}\right)V_y U_{yy}\right]\right\} \tag{32}
$$

$$+ \, \varepsilon \Bigg[\sqrt{\frac{\gamma \pi}{2}} \, M_0 \, \mathrm{Kn}_0 \left(\frac{p_0}{p} \right) \left(\frac{\omega_2}{2} U U_{yxy} + \frac{\omega_2}{2} V U_{yyy} \right)$$

$$- \, \mathrm{Re}(\rho U U)_x - \mathrm{Re}(\rho U V)_y \Bigg]$$

$$- \, \varepsilon \Bigg\{ \frac{\gamma \pi}{2} \, \mathrm{Kn}_0^2 \, M_0^2 \left(\frac{p_0}{p} \right)^2 \Bigg[\left(\frac{\omega_1}{2} - \frac{7\omega_2}{2} + \frac{\omega_6}{6} \right) P_y U_x U_y$$

$$+ \, \frac{\omega_2}{2} P_y U U_{yx} + \frac{\omega_2}{2} P_y V U_{yy} \Bigg] \Bigg\} \qquad \begin{array}{c} (32) \\ (\textit{Cont.}) \end{array}$$

Burnett Y-momentum equation including $\mathcal{O}(\varepsilon)$ terms:

$$P_y \Bigg[1 + \left(\frac{\omega_6}{12} - \frac{2\omega_2}{3} \right) \frac{\gamma \pi}{2} \, \mathrm{Kn}_0^2 \, M_0^2 \left(\frac{p_0}{p} \right)^2 (U_y)^2 \Bigg]$$

$$= \left(\frac{\omega_6}{6} - \frac{4\omega_2}{3} \right) \sqrt{\frac{\gamma \pi}{2}} \, M_0 \, \mathrm{Kn}_0 \left(\frac{p_0}{p} \right) U_y U_{yy}$$

$$+ \, \varepsilon \Bigg[- \sqrt{\frac{\gamma \pi}{2}} \, M_0 \, \mathrm{Kn}_0 \left(\frac{p_0}{p} \right) \left(\frac{\omega_2}{2} \right) (U U_{yx})_y + U_{xy} + V_{yy} \Bigg]$$

$$- \, \varepsilon \Bigg\{ \frac{\gamma \pi}{2} \, \mathrm{Kn}_0^2 \, M_0^2 \left(\frac{p_0}{p} \right)^2 \Bigg[\left(\frac{\omega_2}{2} \right) (P_x V U_{yy} + P_x U U_{xy})$$

$$+ \left(\frac{\omega_1}{2} - \frac{\omega_2}{6} + \frac{\omega_6}{6} \right) P_x V_y U_y \Bigg] \Bigg\}$$

$$+ \, \varepsilon \Bigg[\frac{\gamma \pi}{2} \, \mathrm{Kn}_0^2 \, M_0^2 \left(\frac{p_0}{p} \right)^2 \left(\frac{\omega_2}{3} \right) P_y U U_{xy} \Bigg] \qquad (33)$$